



1 Small-scale dispersion in the presence of Langmuir circulation

2 Henry Chang*, Helga S. Huntley, A. D. Kirwan, Jr.

3 *School of Marine Science and Policy, University of Delaware, Newark, Delaware, USA*

4 Daniel F. Carlson

5 *Department of Earth, Ocean, and Atmospheric Science, Florida State University, Tallahassee,
6 FL, USA; Arctic Research Centre, Department of Bioscience, Aarhus University, Aarhus,
7 Denmark*

8 Jean A. Mensa

9 *formerly: Department of Geology and Geophysics, Yale University, New Haven, CT, USA*

10 Sanchit Mehta, Guillaume Novelli, Tamay M. Özgökmen

11 *Ocean Sciences Department, Rosenstiel School of Marine and Atmospheric Science, University
12 of Miami, Miami, FL, USA*

13 Baylor Fox-Kemper, Brodie Pearson, Jenna Pearson

14 *Department of Earth, Environmental and Planetary Sciences, Brown University, Providence, RI,
15 USA*

16 Ramsey R. Harcourt

17 *Department of Ocean Physics, Applied Physics Laboratory, University of Washington, Seattle,
18 WA, USA*

¹⁹

Andrew C. Poje

²⁰

Department of Mathematics, City University of New York, Staten Island, NY, USA

²¹ *Corresponding author address: School of Marine Science and Policy, University of Delaware,

²² Newark, DE 19716, USA.

²³ E-mail: changhenry@gmail.com

ABSTRACT

24 We present an analysis of ocean surface dispersion characteristics, on 1-
25 100 m scales, obtained by optically tracking a release of $\mathcal{O}(600)$ bamboo
26 plates for 2 hours in the Northern Gulf of Mexico. Under sustained 5-
27 6 m/s winds, energetic Langmuir cells are clearly delineated in the spatially
28 dense plate observations. Within 10 minutes of release, the plates collect in
29 windrows with 15 m spacing aligned with the wind. Windrow spacing grows,
30 through windrow merger, to 40 m after 20 minutes and then expands at a
31 slower rate to 50 m. The presence of Langmuir cells produces strong horizon-
32 tal anisotropy and scale dependence in all surface dispersion statistics com-
33 puted from the plate observations. Relative dispersion in the crosswind direc-
34 tion initially dominates but eventually saturates, while downwind dispersion
35 exhibits continual growth consistent with contributions from both turbulent
36 fluctuations and organized mean shear. Longitudinal velocity differences in
37 the crosswind direction indicate mean convergence at scales below the Lang-
38 muir cell diameter and mean divergence at larger scales. Although the second-
39 order structure function measured by contemporaneous GPS-tracked surface
40 drifters drogued at ~ 0.5 m shows persistent $r^{2/3}$ power law scaling down to
41 100-200 m separation scales, the second-order structure function for the very
42 near surface plates observations has considerably higher energy and signifi-
43 cantly shallower slope at scales below 100 m. This is consistent with con-
44 temporaneous data from undrogued surface drifters and previously published
45 model results indicating shallowing spectra in the presence of direct wind-
46 wave forcing mechanisms.

47 **1. Introduction**

48 Dispersive processes can quickly redistribute both natural and anthropogenic tracer materials
49 in the ocean, thereby impacting a wide range of practical and scientific concerns, from spill con-
50 tainment options to biological productivity. Because these processes involve complex interactions
51 and operate over scales ranging from molecular to the mesoscale, a comprehensive theoretical de-
52 scription has yet to be achieved. Some progress has been made connecting the mesoscale with
53 submesoscales (McWilliams 2016; Kunze 2019). However, much remains unanswered, especially
54 as it relates to even smaller scales near the ocean surface, which are the focus here. These have
55 classically been approached from the perspective of turbulence theory. However, some of the un-
56 derlying assumptions, such as homogeneity and isotropy, may not hold in an ocean environment,
57 particularly near the surface. Consequently, much of what is known of the ocean's dispersive
58 properties derives from empirical analyses (Okubo 1971; Poje et al. 2014; Rypina et al. 2016;
59 Poje et al. 2017; Zavala Sansón et al. 2017). Here we report on quantitative dispersion estimates
60 obtained from a unique dataset capturing trajectories at unusually small scales for an open ocean
61 experiment.

62 Ocean dispersion experiments include both dye and drifter methodologies. Dye experiments
63 generate concentration measurements and provide insight into turbulent mixing coefficients (e.g.,
64 Okubo 1971; Sullivan 1971; Anikiev et al. 1985; Watson and Ledwell 2000; Takewaka et al. 2003;
65 Ledwell et al. 2016). Drifter dispersion studies generally focus on separation statistics of hypothet-
66 ical fluid particles approximated by drifters and floats (e.g., LaCasce 2008, and references cited
67 therein).

68 Both methods pose technical challenges, which boil down to limitations in the time and space
69 scales that can be observed and the accuracy of the measurements. Quantitative measurements of

dye concentrations rely on discrete ship-based samples (e.g., Watson et al. 2013; Ledwell et al. 2016). Drifter observations can be obtained autonomously using GPS at the surface or sonar sub-surface (Lumpkin et al. 2017; LaCasce 2008). This permits sampling over a larger area and longer times. However, GPS uncertainty, alongside cost and logistical considerations, limits the lower end of the time and space scales over which they can be used for dispersion studies (Haza et al. 2014).

Dispersion estimates have been obtained for many areas of the world's oceans including global surveys (Roach et al. 2018), the North Pacific (Kirwan et al. 1978; Zhurbas and Oh 2004), the Atlantic (LaCasce and Bower 2000; Ollitrault et al. 2005; Lumpkin and Eliot 2010), the Arctic (Koszalka et al. 2009; Mensa et al. 2018), the Southern Ocean (LaCasce et al. 2014; Balwada et al. 2016b), the Mediterranean (Lacorata et al. 2001; Schroeder et al. 2012), and the Australian (Mantovanelli et al. 2012), Finish (Torsvik and Kalda 2014), and French (Porter et al. 2016) coasts. Substantial work has also been done in the Gulf of Mexico (e.g. LaCasce and Ohlmann 2003; Poje et al. 2014; Beron-Vera and LaCasce 2016; Zavala Sansón et al. 2017). However, due to the experimental constraints, little information is available on open ocean dispersion over time and space scales on the order of minutes and meters. Yet these scales are critical for the dispersion of pollutants such as oil and relevant to small-scale dynamics near oceanic fronts (D'Asaro et al. 2018). Here we seek to begin to fill that gap, using an innovative dataset of optically tracked floating bamboo plates (Carlson et al. 2018), which provides higher space and time resolution for the trajectories than available from classic Lagrangian drifter and float data.

Specifically, we focus on the dispersive properties during a Langmuir event. Langmuir circulation (LC) is characterized by counter-rotating vortices aligned with the wind direction (Leibovich 1983) and results from an interaction of the wind with the wave field (Fig. 1). The phenomenon is important for dispersion, as it traps floating matter in narrow convergence zones at the surface

94 (Thorpe 2004) and enhances vertical mixing of neutrally buoyant material and water properties
95 (Kukulka et al. 2009; McWilliams and Sullivan 2000). Its dispersive properties have been primar-
96 ily studied in models (e.g., Yang et al. 2015; Kukulka and Harcourt 2017; Shrestha et al. 2018)
97 and generally from an Eulerian perspective. A few attempts have been made to derive estimates
98 of diffusivities from sonar observations, which are thought to detect bubble bands associated with
99 Langmuir circulation, from which velocities are derived (Thorpe et al. 1994; Li 2000).

100 The present study centers on particle-pair statistics, reporting relative dispersion and relative
101 velocity statistics, and presenting velocity structure functions. This approach places the small-
102 scale Lagrangian observations within the context of turbulence theory and permits direct (though
103 limited) comparison with comparable observations from contemporaneous surface GPS-tracked
104 drifters at larger scales. This extends previous work on near-surface structure functions using
105 drifters with resolution down to approximately 100 m (Poje et al. 2014; Balwada et al. 2016a; Poje
106 et al. 2017; Mensa et al. 2018).

107 Velocity fields in Langmuir circulation are well known to be anisotropic (e.g., Thorpe 2004).
108 We quantify the anisotropies in the dispersion and identify convergence scales using the struc-
109 ture functions. The findings can inform future modeling and experimental studies by providing
110 observed statistics as a baseline.

111 Details of the experimental setup are given in the next section. As for most optical techniques,
112 custom tracking algorithms were developed to process the data. These are based on the method-
113 ology described in Carlson et al. (2018), and Section 3 provides a summary. The cumulative
114 effect of uncertainties in the camera position and orientation on the derived statistics is discussed
115 in Appendix A. Results are presented in Section 4, followed by a summary and conclusions in
116 Section 5.

¹¹⁷ **2. Experimental Setup**

¹¹⁸ *a. LASER*

¹¹⁹ The LAgrangian Submesoscale ExpeRiment (LASER) (D'Asaro et al. 2018) was a large, coor-
¹²⁰ dinated effort to study the transport properties of the DeSoto Canyon region in the northern Gulf
¹²¹ of Mexico (Fig. 2). The expedition lasted from 18 January to 13 February 2016. It relied on two
¹²² main vessels, the *R/V Walton Smith*, equipped with a modern suite of instruments and the 110-
¹²³ foot offshore supply boat *Masco VIII*, which was retrofitted to collect meteorological data, while
¹²⁴ primarily serving as platform for drifter releases and aerostat operations.

¹²⁵ *b. Plate Experiments*

¹²⁶ The present analysis is based on trajectories of bamboo plates, observed from an aerostat teth-
¹²⁷ ered to a station-keeping ship, the Ship-Tethered Aerostat Remote Sensing System (STARSS,
¹²⁸ Carlson et al. 2018), illustrated in Fig. 3. The plates were chosen because they are cheap,
¹²⁹ biodegradable, and positively buoyant with nominally no windage. The plates have a diameter
¹³⁰ of 28 cm, draft of 1.75 cm, and thickness of 2 mm. Prior to the field experiment, they were tested
¹³¹ for their float properties and ease of detection in imagery. Within a few minutes of being in the
¹³² ocean, these plates soak up sufficient water to become submerged to 1 – 2 cm depth , with neg-
¹³³ ligible extent above the surface that could be subject to direct wind forcing. While waves can
¹³⁴ flip the plates upside down, orientation was not found to affect the float properties in wave tank
¹³⁵ experiments. The main downside of using plates to measure surface currents is the relatively large
¹³⁶ effort required first to track the plates visually and then to extract accurate trajectories from the
¹³⁷ imagery; see Section 3 for details. In addition, the observational window is limited by the time the

¹³⁸ camera can be kept aloft with the plates within its field of view, and nighttime observations are not
¹³⁹ possible.

¹⁴⁰ As part of LASER, hundreds of plates were released in a series of sub-experiments. FAA regu-
¹⁴¹ lations restricted operations to the box indicated in Fig. 2. The bamboo plates were tossed into the
¹⁴² ocean from a small boat. About half were painted using red, yellow, and magenta biodegradable
¹⁴³ paint (Fig. 3d) to contrast with the ocean surface and to help distinguish between plates. Unpainted
¹⁴⁴ plates were a light beige color (Fig. 3c). A high resolution (8688 x 5792 pixel) color image was
¹⁴⁵ taken every 15 sec. The lens was set to a 17 mm focal length. The aerostat, a helium-filled balloon,
¹⁴⁶ was tethered at an altitude of about 150 m, resulting in a field of view (FOV) of approximately
¹⁴⁷ 320 m × 210 m. Total flight times per experiment for the aerostat were about 3 to 4 hours. This
¹⁴⁸ resulted in just under 2.5 hours of usable trajectories during the Langmuir event on 6 February
¹⁴⁹ 2016.

¹⁵⁰ The camera look angles, ship speed, and ship heading were adjusted to keep the bamboo plates
¹⁵¹ in the camera FOV as they drifted and dispersed. The GPS-INS (Inertial Navigation System)
¹⁵² recorded the camera position and angle at 5 Hz. This information is used for absolute georectifi-
¹⁵³ cation (see Section 3). The *Masco VIII* was equipped with two GT31 GPS units, recording ship
¹⁵⁴ position at 1 Hz. Environmental data was collected from the weather stations on the *Masco VIII*
¹⁵⁵ and the *R/V Walton Smith*, as well as from mobile platforms.

¹⁵⁶ The focus here is on the experiment from the afternoon of 6 February 2016 (all times reported as
¹⁵⁷ local time, CST). Plates were deployed along two tracks perpendicular to the wind direction over
¹⁵⁸ less than 8 minutes, forming a 150 m (crosswind) × 30 m (downwind) patch of approximately
¹⁵⁹ uniform density with 1 plate per 8 m² (Fig. 5a). Their motion was tracked for about 2.5 hours.

¹⁶⁰ c. *Surface Drifters*

¹⁶¹ During LASER, over 1000 CARTHE-type surface drifters (Novelli et al. 2017) were deployed
¹⁶² in multiple groups. They reported their GPS positions nominally every 5 min. Initially, they were
¹⁶³ drogued at 0.5 m, but many lost their drogues during rough storm events. This resulted fortuitously
¹⁶⁴ in a second, distinct set of surface drifters consisting only of a float, that extended about 5 cm into
¹⁶⁵ the water column (Haza et al. 2018). In Section 4d, we report on the statistics of both sets from
¹⁶⁶ a deployment on 21 January 2016, approximately two weeks prior to the plate experiment. The
¹⁶⁷ sampling window chosen here is a calm 3-day period, 1 – 4 February 2016, exhibiting similar wind
¹⁶⁸ conditions to those seen during the plate experiment and preceding the drifters accumulating along
¹⁶⁹ a density front. By this time, the drifters — 300 drogued and 168 undrogued — were dispersed
¹⁷⁰ over a 300 km × 100 km region in the Northern Gulf of Mexico (Fig. 2).

¹⁷¹ d. *Environmental Conditions*

¹⁷² During the 2.5 hours of the experiment on February 6, wind speed was steady between 5 – 7
¹⁷³ m/sec from the north, and net surface heat flux decreased from slight heating to cooling (Fig. 4a).
¹⁷⁴ Potential density ρ profiles derived from conductivity-temperature-depth (CTD) measurements
¹⁷⁵ from the *R/V Walton Smith* (Fig. 4b) indicate a mixed layer depth of approximately 40 – 50 m
¹⁷⁶ and a second stronger pycnocline around 70 – 80 m. The temperature profile at 16:37 reveals an
¹⁷⁷ additional gradient at 20 – 30 m depth. This depth corresponds to the dominant Langmuir cell
¹⁷⁸ diameter during this experiment, as will be described in Section 4.

¹⁷⁹ Two wave buoys deployed near the plates provided the wave spectrum, height, and direction.
¹⁸⁰ The wave buoy data were processed using methods described in Thomson et al. (2018). Data
¹⁸¹ from one of the buoys was eliminated, since it was found to have too much low frequency noise.
¹⁸² For the remaining buoy, only data from intermediate frequencies (0.15 – 0.50 Hz) were kept due

183 to directional incoherence at the lower and higher frequencies. Significant wave heights overall
184 were $0.67 - 0.80$ m and somewhat lower ($0.56 - 0.71$ m) within this frequency band, compared
185 with predictions of $0.5 - 1.0$ m for the significant wave heights at the Pierson-Moskowitz limit
186 (Young 1999) for observed wind speeds. The spectrally weighted wave direction differs by about
187 30 degrees from the wind direction measured simultaneously on the *R/V Walton Smith* 1 km to the
188 SSE, as shown in Fig. 4c.

189 To calculate the average profile of Stokes drift from the observed spectrum after Kenyon (1969),
190 the contributions from frequencies above the resolved 0.5 Hz must be estimated. For this pur-
191 pose, we assume f^{-4} frequency scaling of the energy spectrum extends to $f_x = 4f_p$, where
192 $f_p = g/(2.4\pi U_{10})$ is the peak frequency in a fully developed sea state, and extends above f_x
193 as f^{-5} . An f^{-4} wind sea scaling enhances surface Stokes drift, a transition to f^{-5} scaling
194 around $4f_p$ is selected because recent observations of f^{-4} scaling behavior in more well-resolved
195 spectra (Thomson et al. 2013) are limited to approximately this range. This rather conserva-
196 tive assumption for the scale of a transition at f_x implies that the Stokes drift spectrum between
197 0.5 Hz and f_x continues as f^{-1} , and above f_x as f^{-2} . The resulting average Stokes drift profile
198 is shown in Fig. 4d. With a surface Stokes drift of $U_S = 4.67 \pm 0.49$ cm/sec and shear velocity of
199 $u^* = \sqrt{\tau_0/\rho_0} = 0.66 \pm 0.07$ cm/sec (measured from the *R/V Walton Smith*), the turbulent Lang-
200 muir number is $La_t = \sqrt{u^*/U_S} = 0.38 \pm 0.03$, which falls within the range of values conducive to
201 Langmuir turbulence (McWilliams et al. 1997; Harcourt and D'Asaro 2008; Belcher et al. 2012).
202 The high-frequency tail contribution to this estimate is large, comprising on average 54% of the
203 surface Stokes drift. Alternative parameterizations of Langmuir turbulence, such as the Surface
204 Layer Langmuir number (Harcourt and D'Asaro 2008), are less sensitive to the tail contribution
205 and also place these conditions in a range conducive to Langmuir turbulence.

206 CTD surveys in the nearby area earlier on February 6 reveal weak lateral density gradients,
207 implying weak frontal and submesoscale activity. Therefore, Langmuir circulation should be the
208 dominant dynamic feature present in the small scales measured during the plate experiment.

209 **3. Data Processing**

210 Before attempting any quantitative analysis of the data, the raw images have to be processed by
211 (1) detecting plates, (2) converting pixel coordinates to physical coordinates, and (3) linking plates
212 between images. The procedure is a modification of that described in Carlson et al. (2018) and is
213 briefly summarized below.

214 *a. Plate Detection*

215 The first step in image processing is to mask out swaths along the edges of the photos that are
216 known to contain problematic elements (the ship and sunglint) and are not likely to contain plates.
217 The small boat used for deployment is masked manually. Plates are then identified iteratively in
218 each image using (i) their color, (ii) their size and shape, and (iii) their persistence to distinguish
219 them from other features such as sun glinter, white caps, and seaweed.

220 Taking advantage of the plates' primarily yellowish and reddish colors, thresholding is per-
221 formed on the RGB color channels r , g , and b based on the intensity function

$$F_c = (r - b)^2 + (r - g)^2 + (b - g)^2. \quad (1)$$

222 Pixels in the image with $F_c < 0.05 \max(F_c)$ are masked out. Preliminary plate center estimates
223 are then detected as peaks in the total intensity field, with a minimum intensity of 10% of the
224 maximum total intensity in the particular image and a minimum separation distance of 6 pixels.
225 Since the plate diameter is roughly 8 pixels, the plate centers were then refined as the centroids
226 of intensity-weighted circular patches around each preliminary point with diameter of 9 pixels.

227 Our implementation is based on that by Eric Dufresne and Daniel Blair (<http://site.physics.georgetown.edu/matlab/>), which in turn is based on software by John Crocker, David Grier,
228
229 and Eric Weeks (<http://www.physics.emory.edu/faculty/weeks/idl/>).

230 At the start of subsequent rounds of detection, 5-pixel-radii circles centered on each identified
231 plate are masked and a shape filter is applied by convolving the masked total intensity field with
232 a kernel constructed by applying a 42-by-42 pixel Gaussian lowpass filter with standard deviation
233 of 3 pixels (as implemented in Matlab's `imgaussfilt.m`) to a 2D step function that is 1 in a disk
234 of radius 4 pixels and otherwise 0 . After the first round, the minimum separate distance between
235 plate center candidates is set to 4 pixels. Moreover, the total convolved intensity of the pixel at the
236 center and of those surrounding it up to 2 pixels away must meet two thresholds: It must exceed
237 80% of the maximum value of the filtered total intensity field and 20% of the integral of the kernel.

238 Detection is stopped when no additional plates are identified.

239 *b. Position Rectification*

240 The detected plates are first referenced as pixel coordinates in each image. A high-quality Canon
241 lens was used with a full-frame DSLR, resulting in minimal image distortion, allowing the approx-
242 imation with a pinhole camera model (Kannala et al. 2008). With this assumption, given position
243 and orientation of the camera , the pixel coordinates are converted to real-world coordinates on a
244 flat ocean surface (Mostafa and Schwarz 2001). This is termed absolute rectification.

245 Unfortunately, the heading data for the experiment analyzed here was not accurately recorded,
246 which may also have contaminated the other INS data. Therefore, a relative rectification step was
247 added. This process translates and rotates and potentially dilates the entire plate position field so
248 that the sum of distances between each plate in one frame and the nearest plate in the next frame
249 is minimized. Our implementation used the MATLAB functions `knnsearch` and `fminsearch` for

250 the nested optimization problem. The initial guess centers the field of plates on the origin and
251 aligns its main axis of variability with the x -axis. In the sum of distances, the largest 10% are
252 excluded to avoid contamination from erroneous “plates” (i.e. sun glint).

253 Relative rectification was used to improve the time syncing between images and INS data (by
254 comparing dilation factors to the measured altitude time series), to determine bias corrections for
255 pitch and roll, to remove false positives (by removing plates that moved more than 3.4 m/ 15 sec
256 in the relatively rectified images), and to precondition the linking (see next section). For the latter
257 two purposes, dilation was not included. Relative rectification and outlier removal was performed
258 twice to remove the impact of outliers on the rectification. Relative rectification removes absolute
259 position and velocity information. However, it does not impact the relative motion needed for the
260 analyses in this paper .

261 *c. Plate Linking*

262 Linking is required to connect individual plates between images so as to obtain plate trajec-
263 tories. Most linking algorithms involve a global minimization of distance between associated plates.
264 We used a MATLAB linking algorithm called “Simple Tracker” by J.-Y. Tinevez (<https://www.mathworks.com/matlabcentral/fileexchange/34040-simple-tracker>). After link-
265 ing, plate velocities are estimated from forward finite differencing. Any link implying a velocity
266 greater than 2 standard deviations from the average velocity in its neighborhood is eliminated.
267 This is necessary, because the number of plates detected may change from image to image: Plates
268 exit the camera field of view or are not detected, while sun glint produces false identifications.
269 Our experimental and processing techniques minimize but cannot fully eliminate these issues. For
270 this data set, complete trajectories were obtained for approximately 20% of the 600 plates, using a
271 maximum linking distance of 3.4 m and a maximum gap of 8 image frames. These are the approx-

imately 120 plates used in the relative dispersion calculations in Section 4b. Data for all 600 plates can be used for the average velocity calculations (Section 4a) and structure function calculations (Section 4d), which do not require full trajectories. For this we linked using a maximum linking distance of 1.7 m and a maximum gap of 1 image frame. A shorter maximum linking distance reduces the maximum allowable velocity but produces fewer erroneous links.

4. Results

a. Observations of Langmuir Circulation

Fig. 5 shows five snapshots of the rectified plate positions. Consistent with the presence of Langmuir circulation (LC), the initially uniformly distributed buoyant plates cluster along convergence zones. After 10 min (Fig. 5b), convergence zones with approximately 15-m spacing are visible. Over the next 10 minutes, some of the neighboring windrows approach each other and merge (see animation in supplemental material in the online version of this paper), so that after 20 min (Fig. 5c), the visible convergence zones are spaced approximately 40 m apart. This secondary merging of plates suggests the presence of LC with different magnitudes and length scales, where the initial spacing (Fig. 5b) reveals smaller scale LC and the secondary spacing (Fig. 5c) is driven by stronger, larger scale LC. After 30 min (Fig. 5d), this spacing remains evident. After 125 min (Fig. 5e), convergence zones have separated slightly to approximately 50-m spacing. This final slow growth in spacing coincides with a transition from net surface heating to cooling in the late afternoon (Fig. 4a). The persistent 40 – 50 m window spacing implies a dominant LC cell diameter of 20 – 25 m (see Fig. 1), reflecting a well mixed layer of the same depth, evident in the temperature profile at 16:37 in Fig. 4b. In addition to the evolution of crosswind spacings, plates

294 spread in the downwind direction from 30 m extent (Fig. 5a) to 100 m (Fig. 5e). Windrows are
295 approximately aligned with wind directions.

296 Convergence zone spacing changed rapidly from 15 m (Fig. 5b) to 40 m (Fig. 5c) over the course
297 of just 10 minutes. These multiple convergence zone spacings are evidence that LC is composed of
298 the superposition of many scales of motion, an idea first proposed by Langmuir (1938), of which
299 the dominant scale results in a LC cell diameter of 20 m (corresponding to the 40-m spacing).
300 Alternatively, the dominant LC cell diameter may have grown in time from 7 m (corresponding
301 to the 15-m spacing) to 20 m. However, this is less likely since the 10-minute period over which
302 we observe the change in spacing is much faster than expected for LC evolution, and there is no
303 significant change in wind speed, wind direction, or wave direction over the course of the 2.5 hour
304 experiment (Fig. 4).

305 Clearly, the plates experienced anisotropic dispersion. This is illustrated by expressing our sub-
306 sequent analyses in downwind (x) and crosswind (y) directions.

307 While the plate observations are significantly biased towards convergence zones, the spatial data
308 density allows estimates of the average crosswind structure of the surface velocity field. Fig. 6
309 shows profiles of cumulative plate count, average crosswind velocity, and average downwind ve-
310 locity as functions of crosswind position at both early and late times. The mean quantities repre-
311 sent averages over both time and downwind position of all available observations. The velocities,
312 (u, v) , are taken relative to the moving center of mass of the plate distribution.

313 Early-time results clearly show organized, roughly sinusoidal behavior of the crosswind velocity
314 (v) consistent with counter-rotating Langmuir cells. Regions of high plate accumulation are nearly
315 aligned with convergence zones where $\partial v / \partial y < 0$. The average relative crosswind velocity is 1-
316 2 cm/s, slightly lower than both the 2–3 cm/s crosswind velocities observed on a lake under similar
317 wind conditions by Langmuir (1938) and typical estimates of 1% of the wind speed. The derived

318 velocities are consistent, however, with the early-time evolution from a nearly uniform distribution
 319 to 40m window rows in approximately 20 minutes. Unlike the crosswind velocity, there is very little
 320 discernible pattern in the averaged downwind velocity during the formation period.

321 Later-time results, where downwind averaging occurs over longer spatial scales and data density
 322 outside the convergence zones is low, show the persistence of 1-2 cm/s mean crosswind velocities
 323 with strong correlation between plate density and crosswind convergence. In addition, there is an
 324 organized mean downwind velocity of similar magnitude with peak positive values roughly aligned
 325 with the convergence zones. Sometimes the peak downwind speeds are slightly displaced to the
 326 right, which could be a consequence of the tilting of the window rows relative to the instantaneous
 327 wind direction.

328 *b. Relative dispersion*

329 Relative dispersion is defined as

$$RD(t; l_0) = \langle \|\mathbf{x}_i(t) - \mathbf{x}_j(t)\|^2 \rangle \\ = \frac{1}{N(N-1)} \sum_{i=1}^N \sum_{j \neq i}^N \|\mathbf{x}_i(t) - \mathbf{x}_j(t)\|^2 \quad (2)$$

330 where \mathbf{x}_i are the plate positions, N is the number of plates, $\langle \cdot \rangle$ denotes an average over all plate
 331 pairs, $i \neq j$, $\|\cdot\|$ is the standard Euclidean distance operator, and $l_0 = \langle \|\mathbf{x}_i(t_0) - \mathbf{x}_j(t_0)\| \rangle^{1/2}$ is
 332 the initial rms pair separation. RD is invariant to translation and rotation of the plate field.

333 The downwind RD_x and crosswind RD_y components of relative dispersion are calculated from
 334 the downwind and crosswind separation components, respectively

$$RD_x(t; l_{0x}) = \langle (x_i(t) - x_j(t))^2 \rangle \quad (3)$$

335

$$RD_y(t; l_{0y}) = \langle (y_i(t) - y_j(t))^2 \rangle \quad (4)$$

336 where $l_{0x} = \sqrt{\langle (x_i(t_0) - x_j(t_0))^2 \rangle}$ and $l_{0y} = \sqrt{\langle (y_i(t_0) - y_j(t_0))^2 \rangle}$ are the initial separation scales
 337 in the downwind and crosswind directions, respectively.

338 Fig. 7 shows that RD (black) taken over all possible initial plate pairs, increases with time, al-
 339beit with noticeable fluctuations. Given the pronounced anisotropy in the plate distributions, the
 340 downwind, $RD_x(t; l_{0x})$ (blue), and crosswind, $RD_y(t; l_{0y})$ (red), components of relative dispersion
 341 are also shown for initial separation scales $l_{0x} = l_{0y} = (2.3, 7.8, 15)$ m. For initial separation scales
 342 greater than or equal to the observed, short-time Langmuir cell size, crosswind relative disper-
 343 sion grows faster than the downwind component. At all initial separation scales, however, the
 344 crosswind component eventually saturates. The crosswind saturation level depends on the initial
 345 separation scale. In contrast, while the downwind component of relative dispersion initially grows
 346 slowly (with initial growth rate apparently decreasing with increasing l_{0x}), after ~ 25 minutes all
 347 curves show a significant increase in the growth rate of $RD_x(t; l_{0x})$. On these time-scales, the
 348 downwind dispersion grows like $RD \sim t^2$, rather than the classic Richardson, $RD \sim t^3$ prediction
 349 indicating significant contributions from a mean shear component.

350 Relative diffusivity is estimated by differencing dispersion at two times t_1 and t_2

$$K(l) = \frac{1}{2} \frac{RD(t_2) - RD(t_1)}{t_2 - t_1} \quad (5)$$

351 with corresponding length scale

$$l = \frac{1}{2} \left(RD^{1/2}(t_1) + RD^{1/2}(t_2) \right) \quad (6)$$

352 Values of total relative diffusivity in Table 1 are calculated for early times ($t_1 = 0$ min, $t_2 =$
 353 38 min) and late times ($t_1 = 50$ min, $t_2 = 88$ min) for pairs with initial separation scale $l_0 =$
 354 $\sqrt{l_{0x}^2 + l_{0y}^2} = (3.2, 11.0, 21.3)$ m. At a scale of $l = 39$ m, diffusivity $K = 0.15$ m²/s, somewhat
 355 larger than $K = 0.05 - 0.1$ m²/s from the analysis of dye experiments by Okubo (1971) but within
 356 the range 0.001 – 1 m²/s found by Li (2000) for Langmuir circulation. Fitting the early time

³⁵⁷ diffusivity data gives $K \sim l^{0.52}$, which reflects the slow initial growth in relative dispersion. At late
³⁵⁸ times $K \sim l^{1.15}$, which is in agreement with Okubo (1971).

³⁵⁹ *c. Two-point velocity statistics*

³⁶⁰ For plates i and j , the separation vector is given by

$$\mathbf{r}_{ij}(t) = \mathbf{x}_i(t) - \mathbf{x}_j(t). \quad (7)$$

³⁶¹ The relative velocity is

$$\delta\mathbf{v}_{ij}(t) = \mathbf{v}_i(t) - \mathbf{v}_j(t) = \frac{d}{dt}\mathbf{r}_{ij}(t). \quad (8)$$

³⁶² The longitudinal relative velocity component is defined as

$$\delta v_l = \delta\mathbf{v} \cdot \hat{\mathbf{r}}, \quad (9)$$

³⁶³ and the transverse component is

$$\delta v_t = \|\delta\mathbf{v} \times \hat{\mathbf{r}}\|, \quad (10)$$

³⁶⁴ where dependence on i , j , and t has been dropped from the notation for clarity and $\hat{\mathbf{r}} = \mathbf{r}/\|\mathbf{r}\|$.

³⁶⁵ Note that the longitudinal relative velocity is in general made up of both crosswind and downwind
³⁶⁶ components; likewise for the transverse relative velocity.

³⁶⁷ Like relative dispersion, the longitudinal velocity increment δv_l is invariant to translation and ro-
³⁶⁸ tation of the plate fields. The transverse velocity increment δv_t is invariant to translation but varies
³⁶⁹ with rotation, so we will not use this metric. Fig. 8 shows the normalized probability density
³⁷⁰ functions (PDFs) of the longitudinal velocity increments for three ranges of separation \mathbf{r} . Normal-
³⁷¹ ization is with respect to the standard deviations, approximately 4 cm/sec, 5 cm/sec, and 6 cm/sec
³⁷² for separation scales 0 – 20 m, 40 – 60 m, and 80 – 100 m, respectively. All the PDFs exhibit
³⁷³ Gaussian cores with smaller scales exhibiting larger relative tails, consistent with measurements

at larger scales using surface drifters (Poje et al. 2017). Some uncertainty in the PDFs results from the choice of maximal linking distances: A shorter maximum linking distance reduces the maximum velocity but produces fewer erroneous links, while a longer maximum linking distance allows larger velocities but produces more erroneous links. Thus, heavier tails result from larger allowed linking distances.

d. *Structure functions*

Longitudinal structure functions are the moments of the longitudinal velocity increment

$$S_l^p(r) = \langle (\delta v_l)^p \rangle \quad (11)$$

where $\langle \cdot \rangle$ is now an average over all plate pairs (in space and time) with separation r . Figs. 9 – 10 show the first-order and second-order longitudinal structure functions, respectively. The smallest separation bin is centered at $r = 0.7$ m, with each successive bin center increased by a factor of $\sqrt{2}$, up to $r = 125$ m. Data for smaller bins cannot be obtained reliably, as separation distances become smaller than a plate diameter. Similarly, data for larger bins is questionable due to sampling from the edges of the plate field. Bins with less than 8 pairs per time step are also removed. Errors in the measured camera orientation propagate into structure function errors and are accounted for as described in Appendix A. Additionally, standard errors are calculated to determine confidence intervals.

To evaluate anisotropy in the flow, we examine the longitudinal structure functions conditioned on the separation vector \mathbf{r} being close to the downwind $\hat{\mathbf{x}}$ and crosswind $\hat{\mathbf{y}}$ directions.

$$S_{l_x}^p(r) = \left\langle (\delta v_l)^p \mid |\hat{\mathbf{r}} \cdot \hat{\mathbf{x}}| > 0.98 \right\rangle \quad (12)$$

$$S_{l_y}^p(r) = \left\langle (\delta v_l)^p \mid |\hat{\mathbf{r}} \cdot \hat{\mathbf{y}}| > 0.98 \right\rangle \quad (13)$$

393 The somewhat arbitrary value of 0.98 for the dot product reflects a tradeoff between filtering out
394 data that is not in one of the two primary directions while gathering enough data for meaningful
395 statistics.

396 The first-order structure function S_l^1 is the mean relative velocity as a function of separation r ; it
397 is a measure of the divergent (positive) or convergent (negative) tendency of the flow. This quantity
398 is zero for incompressible homogeneous flows and is approximately so in many other turbulent
399 flows, so traditional turbulent scaling arguments are built around the condition $S_l^1 = 0$. However,
400 the surface velocity field for LC is neither divergence-free nor homogeneous. Additionally, the
401 sampling is spatially inhomogeneous. Therefore, it is not surprising that S_l^1 is non-zero.

402 Fig. 9 shows the first-order structure function S_l^1 at early times (0 – 5 min, solid curves), when the
403 plates are more uniformly distributed, and at later times (15 – 90 min, dashed curves), after most
404 of the plates have reached a quasi-steady windrow configuration (Figs. 5c and 5d). Crosswind and
405 downwind components are indicated by red and blue colors, respectively.

406 If two plates are initially separated by less than the LC cell diameter, they will more likely end
407 up in the same convergence zone and therefore have mean convergence. If two plates are initially
408 separated by more than the LC cell diameter, they will more likely end up in different convergence
409 zones and exhibit mean divergence. This is true up to an initial separation of two LC diameters.

410 See the diagram in Fig. 1.

411 The early-time crosswind component (solid red curve) indicates mean convergence for separa-
412 tions below 7 m and divergence at larger scales, consistent with the first observed windrow spacing
413 of 15 m (Fig. 5b). At later times (dashed red curve), the zero crossing occurs at $r = 20$ m matching
414 the observed convergence zone spacing of approximately 40 m shown in Figs. 5c and 5d. The av-
415 eraged magnitude of crosswind relative velocity is higher at early times when the plate distribution
416 is more homogeneous.

417 In the downwind direction, there is initially (solid blue curve) no significant trend, while at
418 later times (dashed blue curve) there are clear indications of mean divergence, rapidly increasing
419 with the separation distance. This behavior matches the formation of organized mean downwind
420 velocities observed at later times as shown in Fig. 6. The strong anisotropy between the mean
421 crosswind and downwind divergence at later times is also consistent with the slower growth in
422 crosswind relative dispersion compared with downwind relative dispersion in Fig. 7.

423 The second-order structure function was introduced by Kolmogorov (1941b) to describe the
424 inertial range behavior of homogeneous isotropic turbulence. More generally, the second-order
425 structure function is the Fourier cosine transform of the kinetic energy spectrum, whose scale-
426 dependent behavior is related to the nature of the underlying flow. Fig. 10a shows that crosswind
427 S_l^2 is higher at early times (0 – 5 min, solid red curve) than later times (15 – 90 min, dashed
428 red curve). This reflects the initially strong relative motion organizing the plates into Langmuir
429 convergence zones. The disparity arises over almost the entire range of scales, suggesting that LC
430 consists of a superposition of motions from sub-meter through tens of meters. This is consistent
431 with a hierarchy of LC vortices of different sizes first described by Langmuir (1938), as well as
432 with instability mechanisms explaining how the vortices grow (Leibovich 1983). The theory also
433 supports the multiple convergence zone spacings observed in Fig. 5.

434 LC motions are also reflected in the difference between crosswind and downwind S_l^2 , especially
435 at early times. At later times, once the plates are mostly organized into the windrows, the LC cells
436 suppress relative motion on scales less than half their diameter, as is evidenced by the downwind S_l^2
437 exceeding its crosswind counterpart at these scales. Peaks and troughs in the crosswind S_l^2 curves
438 would be expected at separations approximately 1 cell diameter and 2 cell diameters, respectively.
439 At later times, this again suggests cells of size 20 m, while at early times, a multitude of different

440 scales for LC cells are indicated. Peaks and troughs across scales suggest discrete or preferred LC
441 cell sizes, instead of a continuous spectrum.

442 To connect the structure function observations at the small scales ($r < 100$ m) with larger scale
443 dynamics, we also calculated $S_l^2(r)$ from GPS-tracked surface drifters during a calm 3-day period
444 prior to the plate experiment. (See Section 2c for more details about the drifter deployment.)
445 Fig. 10b shows S_l^2 calculated for the drifters and the plates, averaged over all separation directions.

446 At the largest scales ($r > 5$ km), both drogued and undrogued drifters have similar behavior,
447 roughly consistent with standard $S_l^2(r) \sim r^{2/3}$ scaling. At smaller scales, $r < 1 - 2$ km, the drogued
448 and undrogued drifter results diverge, with the undrogued drifters showing a shallowing slope and
449 energy levels consistent with early-time plate results at the largest scales of the plate experiment.
450 Unlike the drifters drogued at ~ 0.5 m depth, the undrogued drifters and the plates exhibit signifi-
451 cantly shallower, $S_l^2(r) \sim r^{1/3}$, scaling at small separation scales. Plates and undrogued drifters are
452 subject to higher shears and wave-induced motion at the very near surface, and undrogued drifters
453 are also more greatly affected by direct windage.

454 The 2/3 power from the drogued drifters is consistent with the inertial range of a forward energy
455 cascade in 3D turbulence (Kolmogorov 1941b,a), an inverse cascade in 2D turbulence (Kraich-
456 nan 1967), and other scalings applicable to oceanic flows (McWilliams 2016). Similar power law
457 behavior was observed using CODE-style drifters (Davis 1985) with one-meter drogue depth de-
458 ployed in summer 2012 in the Northern Gulf of Mexico (Poje et al. 2017). Deviation from this
459 power law for the near surface structure functions (from plates and undrogued drifters) may be
460 attributed to the nature of the observations: the computed structure functions are strictly 2D, in-
461 volving only horizontal differences of horizontal velocity components despite evidence that the
462 vertical to horizontal aspect ratio of the flow approaches unity at these separation scales. In addi-
463 tion, the Lagrangian measurements are inherently biased to over-sampling horizontal convergence

464 zones, and as such may produce different power law behavior than that derived from unbiased
465 Eulerian measurements (Pearson et al. 2019). Despite these limitations, the plate observations
466 clearly indicate a horizontally anisotropic and inhomogeneous flow field with coherent features
467 on 10-100m length scales. The change in the power law behavior of S_l^2 in the very near surface
468 Lagrangian observations is consistent with the distinct shallowing of the kinetic energy spectra at
469 LC-scale waveumbers observed in LES process models (e.g., Hamlington et al. 2014) produced
470 by direct energy input from the wind and waves and propagated up-scale by continual formation
471 and growth of Langmuir cells in the surface layer.

472 **5. Summary and Conclusions**

473 During the LASER field campaign in the northern Gulf of Mexico during January – February
474 2016, several small-scale dispersion experiments were performed using floating bamboo plates
475 observed from a high resolution camera mounted on a helium-filled aerostat. Here the focus is on
476 the experiment that revealed Langmuir streaks roughly aligned with the wind. Individual plates
477 were detected, rectified, and linked to extract their velocities on separation scales of 1 – 100 m.
478 The large number of plates (nearly 600) provided sufficient statistics to evaluate relative dispersion
479 and velocity structure functions.

480 These statistics show clear differences between the downwind and crosswind direction and are
481 consistent with Langmuir circulation. In the crosswind direction, material spreads out on average
482 at scales larger than the dominant Langmuir cell diameters (7 m and 20 m in this experiment) and
483 converges at smaller scales. In the downwind direction perpendicular to the direction of coherent
484 Langmuir cell motions, spreading rate increases with separation distance, which is consistent with
485 turbulent shear dispersion. At larger separation scales, spreading rate in the downwind direction
486 is significantly higher than in the crosswind direction due to the constraining effect of Langmuir

487 circulation. At sub-meter to tens of meter scales, the crosswind component of the second-order
488 structure function is larger than the downwind component; additionally the crosswind component
489 is larger during the early times than the later times, implying Langmuir motions are active simul-
490 taneously at multiple scales, as first hypothesized by Langmuir (Langmuir 1938). The time scales
491 of evolution are too short relative to the changes in the environmental conditions (see Fig. 4) to
492 support the alternate hypothesis of Langmuir cells of a single preferred scale growing over time.

493 The second-order structure function continuously extends results from similar structure func-
494 tions obtained from surface drifter data. Energy input from wind and waves likely alter the mag-
495 nitude and slope of the second-order structure function at small scales and shallow depths. At
496 scales less than 1 km, there are clear differences between the second-order structure function at
497 0.5 m depth (measured by the drogued drifters) and at very shallow 1-5 cm depths (measured by
498 the plates and undrogued drifters) where the structure function has a shallower slope and more
499 energy. This implies that the properties of mesoscale and submesoscale dispersion cannot simply
500 be extrapolated to describe phenomena driven at the small scales, such as Langmuir circulation.

501 We observed differences in early-time velocity statistics, when the plates are more uniformly
502 distributed, and the later-time statistics, when most of the plates have organized into windrows.
503 While the early-time downwind spreading rate S_l^1 is relatively small over all scales, it increases
504 significantly with separation scale at later times. S_l^1 is zero for homogeneous flows, when com-
505 puted from a homogeneous sample, such as on an Eulerian grid; inhomogeneity in the flow or in
506 the sampling method can result in non-zero S_l^1 . At later times, the plates no longer sample the flow
507 uniformly. This impacts the mean statistics (Pearson et al. 2019). Thus, it is important to remem-
508 ber that the “early” versus “late” statistics reflect differential sampling in addition to changes in
509 the underlying flow field.

510 We have shown that inexpensive, biodegradable bamboo plates along with high resolution pho-
511 tography can generate field measurements of small-scale ocean surface dynamics in the open
512 ocean. Analysis of the dispersion characteristics on these scales is essential to unraveling the
513 dynamics across scales and to identifying routes to dissipation in the ocean. This data set pro-
514 vides unique measurements of a Langmuir event which can be directly compared with models
515 for Langmuir circulation. Such comparisons are underway and are expected to lead to improved
516 understanding of Langmuir circulation and validation or improvement of the models.

517 *Acknowledgments.* The authors wish to thank the entire CARTHE LASER team, especially Chief
518 Scientist Eric D’Asaro, for their contribution to a successful field campaign. Weather data was
519 processed by Brian Haus; CTD profiles were produced by Alexander Soloviev and John Kluge;
520 wave buoy data was processed by Jim Thomson; and drifter data was quality controlled and sorted
521 for drogue status by Angelique Haza. We wish to thank Tobias Kukulka and Dong Wang for
522 helpful discussions about Langmuir turbulence, as well as Pablo Huq for helpful discussions
523 about structure functions. This work was made possible by grant support from The Gulf of
524 Mexico Research Initiative for CARTHE and from the Office of Naval Research for CALYPSO
525 (N00014-18-1-2461). All datasets are publicly available through the Gulf of Mexico Research Ini-
526 tiative Information & Data Cooperative (GRIIDC) at <https://data.gulfresearchinitiative.org> under
527 the following DOIs: 10.7266/N7M61H9P (plate observations), 10.7266/N7W0940J (drifter data),
528 10.7266/N7S75DRP, 10.7266/n7-93j3-mn56 (shipboard measurements), and 10.7266/n7-8h5w-
529 nn91 (wave buoy data).

530

APPENDIX A

531

Error Analysis

532 Known error sources for the calculations of S_l^p include imperfect detection (errors in pixel posi-
 533 tion x_p), imperfect rectification (errors in measured camera altitude h , roll θ_r , and pitch θ_p), and
 534 imperfect linking and finite-differencing to find velocities (errors in v_i). Here we focus on the
 535 impact of errors in the measured camera orientation, since these affect the entire field of plates
 536 non-linearly. Other errors are mitigated through outlier removal procedures described in Carlson
 537 et al. (2018).

538 Rectification equations are used to determine physical coordinates (x, y) of each plate relative to
 539 the camera:

$$x = \frac{h \tan(\alpha_x + \theta_r)}{\cos(\alpha_y + \theta_p)} \quad (\text{A1})$$

$$y = \frac{h \tan(\alpha_y + \theta_p)}{\cos(\alpha_x + \theta_r)}, \quad (\text{A2})$$

540 where α_x and α_y are look angles calculated from plate pixel position and intrinsic camera proper-
 541 ties and are assumed to be precisely known. h , θ_r , and θ_p are altitude, roll, and pitch of the camera
 542 measured using the GPS-INS system (described in Section 2b).

543 If the errors δh , $\delta \theta_r$, $\delta \theta_p$ are small relative to h , θ_r , θ_p , then their first-order effect on position
 544 x in physical coordinates is

$$\delta x = \begin{bmatrix} \delta x \\ \delta y \end{bmatrix} = \begin{bmatrix} \partial x / \partial h & \partial x / \partial \theta_r & \partial x / \partial \theta_p \\ \partial y / \partial h & \partial y / \partial \theta_r & \partial y / \partial \theta_p \end{bmatrix} \begin{bmatrix} \delta h \\ \delta \theta_r \\ \delta \theta_p \end{bmatrix} \quad (\text{A3})$$

545 In general the errors are composed of bias plus random components.

$$\delta h(t) = \overline{\delta h} + \delta h'(t) \quad (\text{A4})$$

$$\delta \theta_r(t) = \overline{\delta \theta_r} + \delta \theta'_r(t) \quad (\text{A5})$$

$$\delta \theta_p(t) = \overline{\delta \theta_p} + \delta \theta'_p(t) \quad (\text{A6})$$

546 The bias errors are corrected for during the rectification step of the image processing, leaving the
 547 random errors, which have zero mean.

548 The error in plate separation r_{ij} is

$$\delta \mathbf{r}_{ij} = \delta \mathbf{x}_i - \delta \mathbf{x}_j. \quad (\text{A7})$$

549 We will denote the longitudinal velocity increment as a_{ij} here, to avoid confusion with the error
 550 notation. Recall from equations (8) and (9) that it is defined as

$$a_{ij} = \left(\frac{d}{dt} \mathbf{r}_{ij} \right) \cdot \widehat{\mathbf{r}_{ij}}. \quad (\text{A8})$$

551 With forward finite differencing, this becomes

$$a_{ij} \approx \frac{\mathbf{r}_{ij}(t + \Delta t) - \mathbf{r}_{ij}(t)}{\Delta t} \cdot \widehat{\mathbf{r}_{ij}(t)}. \quad (\text{A9})$$

552 Since the position errors are relatively small, we will neglect the error in $\widehat{\mathbf{r}_{ij}}$, so that the error in
 553 the velocity increment becomes

$$\delta a_{ij} \approx \frac{\delta \mathbf{r}_{ij}(t + \Delta t) - \delta \mathbf{r}_{ij}(t)}{\Delta t} \cdot \widehat{\mathbf{r}_{ij}(t)}. \quad (\text{A10})$$

554 Since $S_l^2 = \langle (a_{ij})^2 \rangle$, the measured second-order structure functions (true plus error) can be writ-
 555 ten in terms of velocity increments and their errors as follows:

$$\begin{aligned} S_l^2 + \delta S_l^2 &= \langle (a_{ij} + \delta a_{ij})^2 \rangle \\ &= \langle a_{ij}^2 \rangle + 2\langle a_{ij} \delta a_{ij} \rangle + \langle \delta a_{ij}^2 \rangle \end{aligned} \quad (\text{A11})$$

556 If the bias errors in altitude, roll, and pitch are zero, and the velocity increment is uncorrelated
 557 with its error δa_{ij} , then the error in S_l^2 is:

$$\delta S_l^2 = \langle \delta a_{ij}^2 \rangle \quad (\text{A12})$$

558 Using (A3), (A7), and (A10),

$$\delta a_{ij} \approx \frac{1}{\Delta t} \left[(c_h \delta h)|_t^{t+\Delta t} + (c_r \delta \theta_r)|_t^{t+\Delta t} + (c_p \delta \theta_p)|_t^{t+\Delta t} \right], \quad (\text{A13})$$

559 where

$$c_h = \frac{\partial \mathbf{x}}{\partial h} \Big|_j^i \cdot \widehat{\mathbf{r}_{ij}}, \quad c_r = \frac{\partial \mathbf{x}}{\partial \theta_r} \Big|_j^i \cdot \widehat{\mathbf{r}_{ij}}, \quad c_p = \frac{\partial \mathbf{x}}{\partial \theta_p} \Big|_j^i \cdot \widehat{\mathbf{r}_{ij}}. \quad (\text{A14})$$

560 Squaring (A13) gives

$$\Delta t^2 \delta a_{ij}^2 = (c_h \delta h|_t^{t+\Delta t} + c_r \delta \theta_r|_t^{t+\Delta t} + c_p \delta \theta_p|_t^{t+\Delta t})^2. \quad (\text{A15})$$

561 The random errors are expected to be uncorrelated in time, with zero cross-correlations, so that

$$\Delta t^2 \langle \delta a_{ij}^2 \rangle = 2(\langle c_h^2 \rangle \langle \delta h^2 \rangle + \langle c_r^2 \rangle \langle \delta \theta_r^2 \rangle + \langle c_p^2 \rangle \langle \delta \theta_p^2 \rangle) \quad (\text{A16})$$

562 There is a factor of 2 here, because there are terms at t and at $t + \Delta t$, each squared separately,
563 but then averaged over all times.

564 S_l^2 is a function of separation scale r . This can be eliminated by integrating S_l^2 over all values of
565 r . We will denote the integrated longitudinal second-order structure function as \mathcal{S} . When $\langle \cdot \rangle$ is
566 computed over a subsample of the time series, the error in \mathcal{S} is a function of the sampling window
567 τ , even though the error statistics for the camera orientation are assumed to be independent of τ .
568 This is because c_h , c_r , and c_p are functions of τ . On the other hand, if there are sufficient samples
569 in a window and the plate motions are statistically stationary, then \mathcal{S} should be independent of τ :

$$\begin{aligned} \mathcal{S} + \delta \mathcal{S}(\tau) &= \mathcal{S} + \frac{2 \int \langle c_h^2 \rangle(\tau) dr}{\Delta t^2} \langle \delta h^2 \rangle \dots \\ &\quad + \frac{2 \int \langle c_r^2 \rangle(\tau) dr}{\Delta t^2} \langle \delta \theta_r^2 \rangle + \frac{2 \int \langle c_p^2 \rangle(\tau) dr}{\Delta t^2} \langle \delta \theta_p^2 \rangle \end{aligned} \quad (\text{A17})$$

570 We compute $\mathcal{S} + \delta \mathcal{S}(\tau)$ directly from the data, using sampling windows spanning 5 frames
571 (1 min). The coefficients of the second, third, and fourth terms on the right-hand side of (A17) can
572 also be computed explicitly. This results in a time series for the right-hand side with four unknown
573 constants, \mathcal{S} , $\langle \delta h^2 \rangle$, $\langle \delta \theta_r^2 \rangle$, and $\langle \delta \theta_p^2 \rangle$. These can be determined by least-squares fitting to the
574 time series $\mathcal{S} + \delta \mathcal{S}(\tau)$. An example of such a fit, using 190 frames (38 non-overlapping sampling
575 windows of 1 min) starting with frame 171, is shown in Fig. 11.

Unfortunately, $\int \langle c_h^2 \rangle(\tau) dr$ is close to constant, resulting in some uncertainty in the estimated values of \mathcal{S} and $\langle \delta h^2 \rangle$. For greater robustness, we repeated the fits for 15 different scenarios, using sampling windows sized 2, 3, 4, 5, and 6 frames and fitting intervals of 120, 160, 180, and 190 frames. (Combinations of these parameters where a fractional number of sampling windows fits into the interval were not used.) The different estimates and their means for $\langle \delta h^2 \rangle$, $\langle \delta \theta_r^2 \rangle$, and $\langle \delta \theta_p^2 \rangle$ are shown in Fig. 12. These means — $\langle \delta h^2 \rangle \approx (0.25 \text{ m})^2$, $\langle \delta \theta_r^2 \rangle \approx (0.45^\circ)^2$, and $\langle \delta \theta_p^2 \rangle \approx (0.45^\circ)^2$ — were used to estimate the errors reported for the second-order structure function. Errors for higher-order structure functions can be similarly estimated. Note that random errors do not affect the first-order structure function.

References

- Anikiev, V., O. Zaytsev, T. Zaytseva, and V. Yabosh, 1985: Experimental investigation of the diffusion parameters in the ocean. *Izv. Atmos. Ocean Phys.*, **21**, 931–934.
- Balwada, D., J. H. LaCasce, and K. G. Speer, 2016a: Scale-dependent distribution of kinetic energy from surface drifters in the Gulf of Mexico. *Geophys. Res. Lett.*, **43** (20), 10,856–10,863, doi:10.1002/2016GL069405.
- Balwada, D., K. G. Speer, J. H. LaCasce, W. B. Owens, J. Marshall, and R. Ferrari, 2016b: Circulation and stirring in the southeast pacific ocean and the scotia sea sectors of the antarctic circumpolar current. *J. Phys. Oceanogr.*, **46** (7), 2005–2027, doi:10.1175/JPO-D-15-0207.1.
- Belcher, S. E., and Coauthors, 2012: A global perspective on Langmuir turbulence in the ocean surface boundary layer. *Geophys. Res. Lett.*, **39**, L18 605, doi:10.1029/2012GL052932.
- Beron-Vera, F. J., and J. H. LaCasce, 2016: Statistics of simulated and observed pair separations in the Gulf of Mexico. *J. Phys. Oceanogr.*, **46** (7), 2183–2199, doi:10.1175/JPO-D-15-0127.1.

- 598 Carlson, D. F., and Coauthors, 2018: Surface ocean dispersion observations from the ship-tethered
599 aerostat remote sensing system. *Front. Mar. Sci.*, **5**, 479, doi:10.3389/fmars.2018.00479.
- 600 D'Asaro, E. A., and Coauthors, 2018: Ocean convergence and the dispersion of flotsam. *Proc.*
601 *Natl. Acad. Sci. USA*, **115** (6), 1162–1167, doi:10.1073/pnas.1718453115.
- 602 Davis, R. E., 1985: Drifter observations of coastal surface currents during CODE: The statistical
603 and dynamical views. *J. Geophys. Res.*, **90** (C3), 4756–4772, doi:10.1029/JC090iC03p04756.
- 604 Hamlington, P. E., L. P. Van Roekel, B. Fox-Kemper, K. Julien, and G. P. Chini, 2014: Langmuir
605 submesoscale interactions: Descriptive analysis of multiscale frontal spindown simulations. *J.*
606 *Phys. Oceanogr.*, **44** (9), 2249–2272, doi:10.1175/JPO-D-13-0139.1.
- 607 Harcourt, R. R., and E. A. D'Asaro, 2008: Large-eddy simulation of Langmuir turbulence in pure
608 wind seas. *J. Phys. Oceanogr.*, **38**, 1542–1562, doi:10.1175/2007JPO3842.1.
- 609 Haza, A. C., T. M. Özgökmen, A. Griffa, A. C. Poje, and M.-P. Lelong, 2014: How does drifter
610 position uncertainty affect ocean dispersion estimates? *J. Atmos. Oceanic Technol.*, **31** (12),
611 2809–2828, doi:10.1175/JTECH-D-14-00107.1.
- 612 Haza, A. C., and Coauthors, 2018: Drogue-loss detection for surface drifters during the Lagrangian
613 Submesoscale Experiment (LASER). *J. Atmos. Oceanic Technol.*, **35** (4), 705–725, doi:10.1175/
614 jtech-d-17-0143.1.
- 615 Kannala, J., J. Heikkilä, and S. S. Brandt, 2008: Geometric camera calibration. *Wiley Encyclopedia*
616 *of Computer Science and Engineering*, B. W. Wah, Ed., American Cancer Society, 1–11, doi:
617 10.1002/9780470050118.ecse589.
- 618 Kenyon, K. E., 1969: Stokes drift for random gravity waves. *J. Geophys. Res.*, **74** (28), 6991–6994,
619 doi:10.1029/JC074i028p06991.

- 620 Kirwan, A. D., Jr., G. J. McNally, E. Reyna, and W. J. Merrell, Jr, 1978: The near-surface
621 circulation of the eastern North Pacific. *J. Phys. Oceanogr.*, **8** (6), 937–945, doi:10.1175/
622 1520-0485(1978)008<0937:TNSCOT>2.0.CO;2.
- 623 Kolmogorov, A. N., 1941a: Dissipation of energy in locally isotropic turbulence. *Dokl. Akad. Nauk*
624 *SSSR*, **32**, 16–18.
- 625 Kolmogorov, A. N., 1941b: The local structure of turbulence in incompressible viscous fluid for
626 very large reynolds number. *Dokl. Akad. Nauk SSSR*, **30**, 9–13.
- 627 Koszalka, I. M., J. H. LaCasce, and K. A. Orvik, 2009: Relative dispersion in the Nordic Seas. *J.*
628 *Mar. Res.*, **67** (4), 411–433, doi:10.1357/002224009790741102.
- 629 Kraichnan, R. H., 1967: Inertial ranges in two-dimensional turbulence. *Phys. Fluids*, **10**, 1417–
630 1423, doi:10.1063/1.1762301.
- 631 Kukulka, T., and R. R. Harcourt, 2017: Influence of Stokes drift decay scale on Langmuir turbu-
632 lence. *J. Phys. Oceanogr.*, **47** (7), 1637–1656, doi:10.1175/JPO-D-16-0244.1.
- 633 Kukulka, T., A. J. Plueddemann, J. H. Trowbridge, and P. P. Sullivan, 2009: Significance of Lang-
634 muir circulation in upper ocean mixing: Comparison of observations and simulations. *Geophys.*
635 *Res. Lett.*, **36**, L10 603, doi:10.1029/2009GL037620.
- 636 Kunze, E., 2019: A unified model spectrum for anisotropic stratified and isotropic turbulence in
637 the ocean and atmosphere. *J. Phys. Oceanogr.*, **49** (2), 385–407, doi:10.1175/JPO-D-18-0092.1.
- 638 LaCasce, J. H., 2008: Statistics from Lagrangian observations. *Prog Oceanogr*, **77** (1), 1–29,
639 doi:10.1016/j.pocean.2008.02.002.
- 640 LaCasce, J. H., and A. Bower, 2000: Relative dispersion in the subsurface North Atlantic. *J. Mar.*
641 *Res.*, **58** (6), 863–894, doi:10.1357/002224000763485737.

- 642 LaCasce, J. H., R. Ferrari, J. Marshall, R. Tulloch, D. Balwada, and K. Speer, 2014: Float-derived
643 isopycnal diffusivities in the dimes experiment. *J. Phys. Oceanogr.*, **44** (2), 764–780, doi:10.
644 1175/JPO-D-13-0175.1.
- 645 LaCasce, J. H., and J. C. Ohlmann, 2003: Relative dispersion at the surface of the Gulf of Mexico.
646 *J. Mar. Res.*, **61** (3), 285–312, doi:10.1357/002224003322201205.
- 647 Lacorata, G., E. Aurell, and A. Vulpiani, 2001: Drifter dispersion in the Adriatic Sea: La-
648 grangian data and chaotic model. *Annales Geophysicae*, **19** (1), 121–129, doi:10.5194/
649 angeo-19-121-2001.
- 650 Langmuir, I., 1938: Surface motion of water induced by wind. *Science*, **87** (2250), 119–123, doi:
651 10.1126/science.87.2250.119.
- 652 Ledwell, J. R., R. He, Z. Xue, S. F. DiMarco, L. J. Spencer, and P. Chapman, 2016: Dispersion
653 of a tracer in the deep Gulf of Mexico. *J. Geophys. Res. Oceans*, **121** (2), 1110–1132, doi:
654 10.1002/2015JC011405.
- 655 Leibovich, S., 1983: The form and dynamics of Langmuir circulations. *Ann. Rev. Fluid Mech.*, **15**,
656 391–427, doi:10.1146/annurev.fl.15.010183.002135.
- 657 Li, M., 2000: Estimating horizontal dispersion of floating particles in wind-driven upper ocean.
658 *Spill Sci. Technol. Bull.*, **6** (3-4), 255–261, doi:10.1016/S1353-2561(01)00044-5.
- 659 Lumpkin, R., and S. Eliot, 2010: Surface drifter pair spreading in the North Atlantic. *J. Geophys.*
660 *Res. - Oceans*, **115** (C12), C12 017, doi:10.1029/2010JC006338.
- 661 Lumpkin, R., T. Özgökmen, and L. Centurioni, 2017: Advances in the application of surface
662 drifters. *Annu. Rev. Mar. Sci.*, **9**, 59–81, doi:10.1146/annurev-marine-010816-060641.

- 663 Mantovanelli, A., M. L. Heron, S. F. Heron, and C. R. Steinberg, 2012: Relative dispersion of
664 surface drifters in a barrier reef region. *J. Geophys. Res. - Oceans*, **117 (C11)**, C11016, doi:
665 10.1029/2012JC008106.
- 666 McWilliams, J. C., 2016: Submesoscale currents in the ocean. *Proc. R. Soc. A*, **472**, 20160117,
667 doi:10.1098/rspa.2016.0117.
- 668 McWilliams, J. C., and P. P. Sullivan, 2000: Vertical mixing by Langmuir circulations. *Spill Sci.
669 Technol. Bull.*, **6 (3-4)**, 225–237, doi:10.1016/S1353-2561(01)00041-X.
- 670 McWilliams, J. C., P. P. Sullivan, and C.-H. Moeng, 1997: Langmuir turbulence in the ocean. *J.
671 Fluid Mech.*, **334**, 1–30, doi:10.1017/S0022112096004375.
- 672 Mensa, J. A., M.-L. Timmermans, I. E. Kozlov, W. W. J., and T. M. Özgökmen, 2018: Surface
673 drifter observations from the arctic ocean’s beaufort sea: Evidence for submesoscale dynamics.
674 *J. Geophys. Res.*, **123**, 2635–2645, doi:10.1002/2017JC013728.
- 675 Mostafa, M. M. R., and K. P. Schwarz, 2001: Digital image georeferencing from a multi-
676 ple camera system by GPS/INS. *ISPRS J. Photogramm. Remote Sens.*, **56 (1)**, 1–12, doi:
677 10.1016/S0924-2716(01)00030-2.
- 678 Novelli, G., C. M. Guigand, C. Cousin, E. H. Ryan, N. J. M. Laxague, H. Dai, B. K. Haus, and
679 T. M. Özgökmen, 2017: A biodegradable surface drifter for ocean sampling on a massive scale.
680 *J. Atmos. Oceanic Technol.*, **34 (11)**, 2509–2532, doi:10.1175/JTECH-D-17-0055.1.
- 681 Okubo, A., 1971: Oceanic diffusion diagrams. *Deep Sea Research and Oceanographic Abstracts*,
682 **18 (8)**, 789–802, doi:10.1016/0011-7471(71)90046-5.
- 683 Ollitrault, M., C. Gabillet, and A. C. De Verdière, 2005: Open ocean regimes of relative dispersion.
684 *J. Fluid Mech.*, **533**, 381–407, doi:10.1017/S0022112005004556.

- 685 Pearson, J., B. Fox-Kemper, R. Barkan, J. Choi, A. Bracco, and J. C. McWilliams, 2019: Impacts
686 of convergence on structure functions from surface drifters in the Gulf of Mexico. *J. Phys.*
687 *Oceanogr.*, **49** (3), 675–690, doi:10.1175/JPO-D-18-0029.1.
- 688 Poje, A. C., T. M. Özgökmen, D. J. Bogucki, and A. D. Kirwan Jr., 2017: Evidence of a forward
689 energy cascade and Kolmogorov self-similarity in submesoscale ocean surface drifter observa-
690 tions. *Phys. Fluids*, **29** (2), 020 701, doi:10.1063/1.4974331.
- 691 Poje, A. C., and Coauthors, 2014: Submesoscale dispersion in the vicinity of the *Deepwater*
692 *Horizon* spill. *PNAS*, **111** (35), 12 693–12 698, doi:10.1073/pnas.1402452111.
- 693 Porter, M., M. E. Inall, J. A. M. Green, J. H. Simpson, A. C. Dale, and P. I. Miller, 2016: Drifter
694 observations in the summer time Bay of Biscay slope current. *J. Marine Syst.*, **157**, 65–74,
695 doi:10.1016/j.jmarsys.2016.01.002.
- 696 Roach, C. J., D. Balwada, and K. Speer, 2018: Global observations of horizontal mixing from
697 argo float and surface drifter trajectories. *J. Geophys. Res.: Oceans*, **123** (7), 4560–4575, doi:
698 10.1029/2018JC013750.
- 699 Rypina, I. I., A. Kirincich, S. Lentz, and M. Sundermeyer, 2016: Investigating the eddy dif-
700 fusivity concept in the coastal ocean. *J. Phys. Oceanogr.*, **46** (7), 2201–2218, doi:10.1175/
701 JPO-D-16-0020.1.
- 702 Schroeder, K., and Coauthors, 2012: Targeted Lagrangian sampling of submesoscale dispersion at
703 a coastal frontal zone. *Geophys. Res. Lett.*, **39** (11), L11 608, doi:10.1029/2012GL051879.
- 704 Shrestha, K., W. Anderson, and J. Kuehl, 2018: Langmuir turbulence in coastal zones: Structure
705 and length scales. *J. Phys. Oceanogr.*, **48** (5), 1089–1115, doi:10.1175/JPO-D-17-0067.1.

- 706 Sullivan, P. J., 1971: Some data on the distance-neighbour function for relative diffusion. *J. Fluid*
707 *Mech.*, **47** (3), 601–607, doi:10.1017/S0022112071001253.
- 708 Takewaka, S., S. Misaki, and T. Nakamura, 2003: Dye diffusion experiment in a longshore current
709 field. *Coast. Engng. J.*, **45** (3), 471–487, doi:10.1142/S0578563403000841.
- 710 Thomson, J., E. A. D'Asaro, M. F. Cronin, W. E. Rogers, R. R. Harcourt, and A. Shcherbina,
711 2013: Waves and the equilibrium range at ocean weather station p. *J. Geophys. Res. - Oceans*,
712 **118** (11), 5951–5962, doi:10.1002/2013JC008837.
- 713 Thomson, J., J. B. Girton, R. Jha, and A. Trapani, 2018: Measurements of directional wave spectra
714 and wind stress from a wave glider autonomous surface vehicle. *J. Atmos. Oceanic Technol.*,
715 **35** (2), 347–363, doi:10.1175/JTECH-D-17-0091.1.
- 716 Thorpe, S. A., 2004: Langmuir circulation. *Annu. Rev. Fluid Mech.*, **36**, 55–79, doi:10.1146/
717 annurev.fluid.36.052203.071431.
- 718 Thorpe, S. A., M. S. Cure, A. Graham, and A. J. Hall, 1994: Sonar observations of Langmuir
719 circulation and estimation of dispersion of floating particles. *J. Atmos. Oceanic Technol.*, **11** (5),
720 1273–1294, doi:10.1175/1520-0426(1994)011<1273:SOOLCA>2.0.CO;2.
- 721 Torsvik, T., and J. Kalda, 2014: Analysis of surface current properties in the Gulf of Finland
722 using data from surface drifters. *Measuring and Modeling of Multi-Scale Interactions in the*
723 *Marine Environment - IEEE/OES Baltic International Symposium 2014, BALTIC 2014*, IEEE,
724 1–9, doi:10.1109/BALTIC.2014.6887845.
- 725 Watson, A. J., and J. R. Ledwell, 2000: Oceanographic tracer release experiments using sulphur
726 hexafluoride. *J. Geophys. Res. - Oceans*, **105** (C6), 14 325–14 337, doi:10.1029/1999JC900272.

- 727 Watson, A. J., J. R. Ledwell, M.-J. Messias, B. A. King, N. Mackay, M. P. Meredith, B. Mills, and
728 A. C. N. Garabato, 2013: Rapid cross-density ocean mixing at mid-depths in the Drake Passage
729 measured by tracer release. *Nature*, **501** (7467), 408–411, doi:10.1038/nature12432.
- 730 Yang, D., B. Chen, M. Chamecki, and C. Meneveau, 2015: Oil plumes and dispersion in Langmuir,
731 upper-ocean turbulence: Large-eddy simulations and K-profile parameterization. *J. Geophys.
732 Res. Oceans*, **120** (7), 4729–4759, doi:10.1002/2014JC010542.
- 733 Young, I. R., 1999: *Wind Generated Ocean Waves*. Elsevier, 288 pp.
- 734 Zavala Sansón, L., P. Pérez-Brunius, and J. Sheinbaum, 2017: Surface relative dispersion
735 in the southwestern Gulf of Mexico. *J. Phys. Oceanogr.*, **47** (2), 387–403, doi:10.1175/
736 JPO-D-16-0105.1.
- 737 Zhurbas, V., and I. S. Oh, 2004: Drifter-derived maps of lateral diffusivity in the Pacific and
738 Atlantic Oceans in relation to surface circulation patterns. *J. Geophys. Res. - Oceans*, **109** (C5),
739 C05 015, doi:10.1029/2003JC002241.

⁷⁴⁰ **LIST OF TABLES**

| | |
|--|----|
| ⁷⁴¹ Table 1. Relative diffusivities K and length scales l calculated from equations (5-6) for ⁷⁴² two time intervals and three initial length scales l_0 . | 39 |
|--|----|

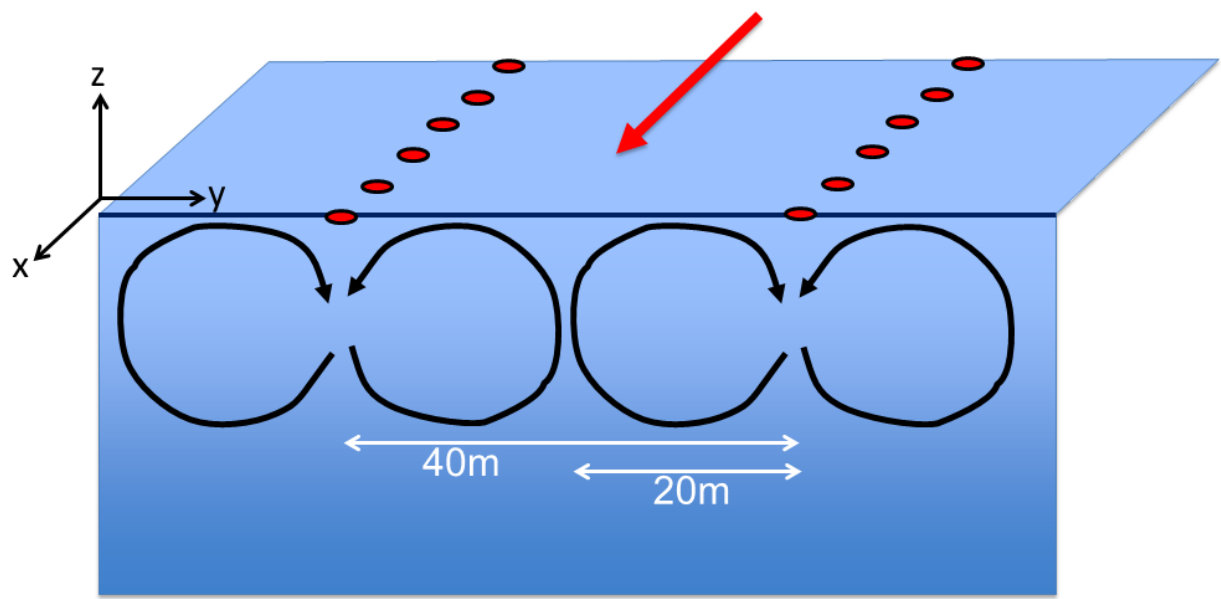
743 TABLE 1. Relative diffusivities K and length scales l calculated from equations (5-6) for two time intervals
 744 and three initial length scales l_0 .

| $l_0(m)$ | Early (0-38 min) | | Late (50-88 min) | |
|----------|------------------|------------|------------------|------------|
| | $l(m)$ | $K(m^2/s)$ | $l(m)$ | $K(m^2/s)$ |
| 3.2 | 9.7 | 0.056 | 24.2 | 0.087 |
| 11.0 | 16.4 | 0.078 | 29.9 | 0.102 |
| 21.3 | 25.4 | 0.092 | 39.1 | 0.150 |

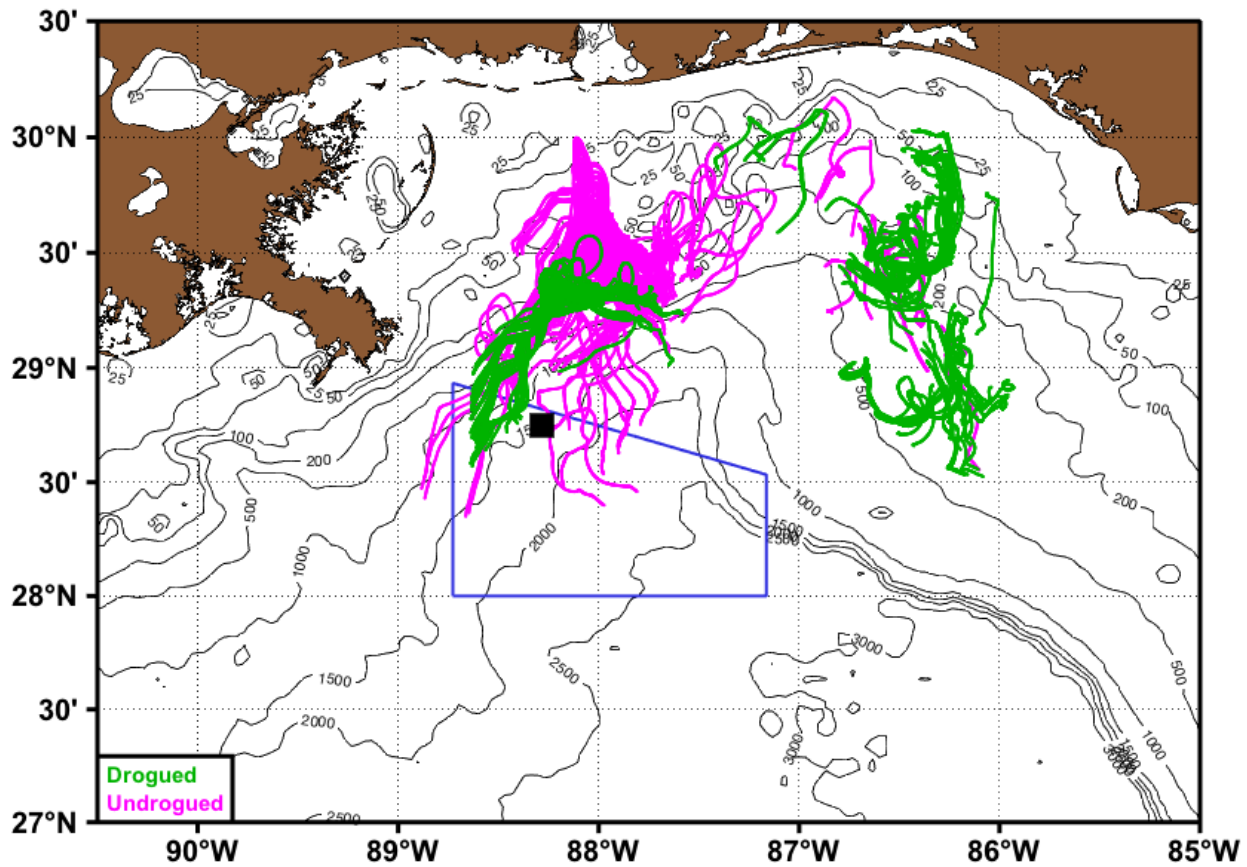
745 LIST OF FIGURES

- 746 **Fig. 1.** Simple diagram of counter-rotating Langmuir circulation cells of 20-m diameter with arrows
747 indicating direction of rotation with wind direction shown by red arrow. Red plates are
748 shown clustered in the convergence zones (above downwelling regions), which are spaced
749 40 m apart. 42
- 750 **Fig. 2.** Northeastern Gulf of Mexico with bathymetry contours. The blue box indicates the area
751 where aerostat operations were permitted. Trajectories of GPS-tracked surface drifters with
752 (green) and without (magenta) drogue from 1 February through 4 February 2016 are shown.
753 The black square marks the location of the Langmuir experiment on 6 February 2016 near
754 28.75° N, 88.28° W. 43
- 755 **Fig. 3.** Experimental set-up. (a) Canon camera, GoPro camera, GPS-INS, and 5 GHz wifi antenna
756 mounted to the aerostat. (b) Aerial view of the aerostat (upper right), ship (lower left), and
757 bamboo plates (middle right). (c) Plates being released in the ocean by small boat. (d) Stack
758 of painted plates. 44
- 759 **Fig. 4.** Environmental conditions on 6 February 2016. (a) Wind speed (blue), and surface heat flux
760 (red) from the *R/V Walton Smith*. (b) CTD temperature and potential density profiles. (c)
761 Wind direction from the *R/V Walton Smith* (blue); spectral averaged wave direction (green)
762 and surface Stokes drift (red) based on wave buoy data. Start and end times of plate obser-
763 vations are indicated in (a) and (c) by black dotted lines. (d) Stokes drift speed (left) and
764 direction (right) calculated from wave buoy data, averaged over the 2.5 hours of the Lang-
765 muir experiment. Directions are reported as where wind, waves, and Stokes drift originate
766 from. 45
- 767 **Fig. 5.** Relatively rectified plate positions after 0, 10, 20, 30, and 125 minutes, respectively, (a)
768 – (e). Black arrows show wind direction inferred from the heading of the aerostat, which
769 was designed to point into the wind. Grid spacing is 10 m in both directions. An animated
770 version of this figure is included as supplemental material in the online version of this paper. 46
- 771 **Fig. 6.** Binned cumulative plate count (black), average crosswind velocity (red-dashed), and aver-
772 age downwind velocity (blue-dashed) as functions of crosswind position, for the first 10 min
773 in (a), and for 50–90 min in (b). The corresponding solid curves are low-pass filtered veloc-
774 ities, with cut-off at 10 m for (a) and cut-off at 20 m for (b). 47
- 775 **Fig. 7.** Relative dispersion as a function of time for initially isotropic pair distributions. Average
776 over all directions and scales (black), in the crosswind direction (red), and in the downwind
777 direction (blue). Gaps reflect frames that could not be successfully processed. 48
- 778 **Fig. 8.** Normalized PDFs of longitudinal velocity increments for 3 separation distance bins. Uncer-
779 tainty is shown (shading) for maximum linking distances of 1.7 – 3.4 m, which correspond
780 to maximum velocities of 11 – 22 cm/sec relative to the mean. A normalized Gaussian is
781 indicated by the black curve. 49
- 782 **Fig. 9.** Longitudinal first-order structure function for crosswind (red) and downwind (blue) compo-
783 nents, subsampled at early (solid) and late (dashed) times. Shaded regions are 95% confi-
784 dence intervals determined from standard error calculations. 50
- 785 **Fig. 10.** Longitudinal second-order structure function. (a) Crosswind (red) and downwind (blue)
786 components, subsampled at early (solid) and late (dashed) times. (b) For early-time (solid
787 black) and late-time (dashed black) plates, plus drogued (green) and undrogued (magenta)

| | | |
|-----|--|----|
| 788 | drifters. Shaded regions are 95% confidence intervals determined from standard error cal- | 51 |
| 789 | culations. | |
| 790 | Fig. 11. Integrated second-order structure function with error (dark blue) as a function of sampling | |
| 791 | window τ (5-frame average) and the best fit for the individual components and their sum of | |
| 792 | the right-hand side of (A17), as computed over 38 sampling windows. | 52 |
| 793 | Fig. 12. Different estimates of the error statistics $\langle \delta h^2 \rangle$, $\langle \delta \theta_r^2 \rangle$, and $\langle \delta \theta_p^2 \rangle$ of altitude, roll, and pitch, | |
| 794 | respectively, from 15 fittings. Mean values are indicated by \times 's. | 53 |



795 FIG. 1. Simple diagram of counter-rotating Langmuir circulation cells of 20-m diameter with arrows indi-
796 cating direction of rotation with wind direction shown by red arrow. Red plates are shown clustered in the
797 convergence zones (above downwelling regions), which are spaced 40 m apart.



798 FIG. 2. Northeastern Gulf of Mexico with bathymetry contours. The blue box indicates the area where
 799 aerostat operations were permitted. Trajectories of GPS-tracked surface drifters with (green) and without (ma-
 800 genta) drogue from 1 February through 4 February 2016 are shown. The black square marks the location of the
 801 Langmuir experiment on 6 February 2016 near 28.75° N, 88.28° W.

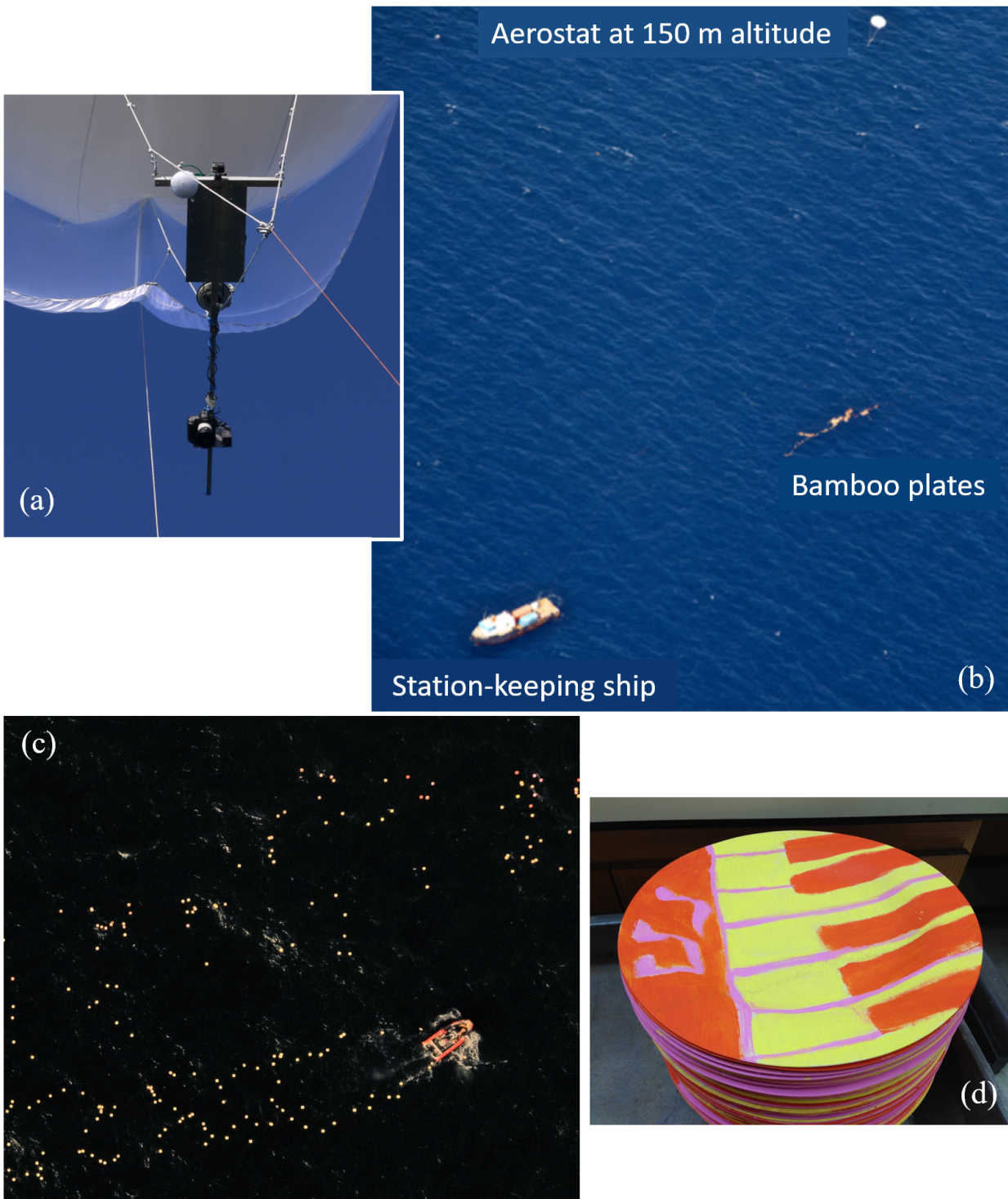


FIG. 3. Experimental set-up. (a) Canon camera, GoPro camera, GPS-INS, and 5 GHz wifi antenna mounted to the aerostat. (b) Aerial view of the aerostat (upper right), ship (lower left), and bamboo plates (middle right). (c) Plates being released in the ocean by small boat. (d) Stack of painted plates.

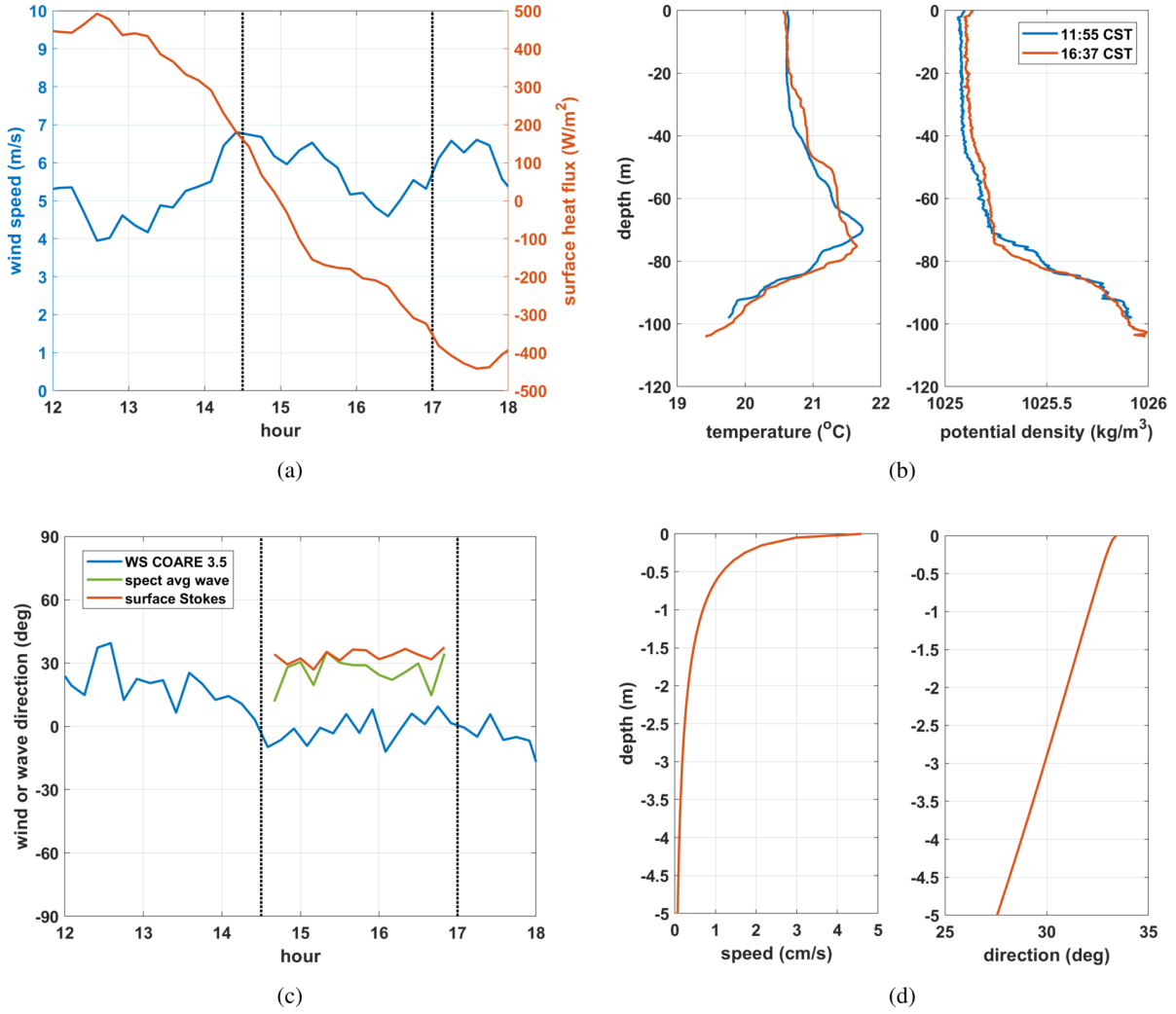


FIG. 4. Environmental conditions on 6 February 2016. (a) Wind speed (blue), and surface heat flux (red) from the *R/V Walton Smith*. (b) CTD temperature and potential density profiles. (c) Wind direction from the *R/V Walton Smith* (blue); spectral averaged wave direction (green) and surface Stokes drift (red) based on wave buoy data. Start and end times of plate observations are indicated in (a) and (c) by black dotted lines. (d) Stokes drift speed (left) and direction (right) calculated from wave buoy data, averaged over the 2.5 hours of the Langmuir experiment. Directions are reported as where wind, waves, and Stokes drift originate from.

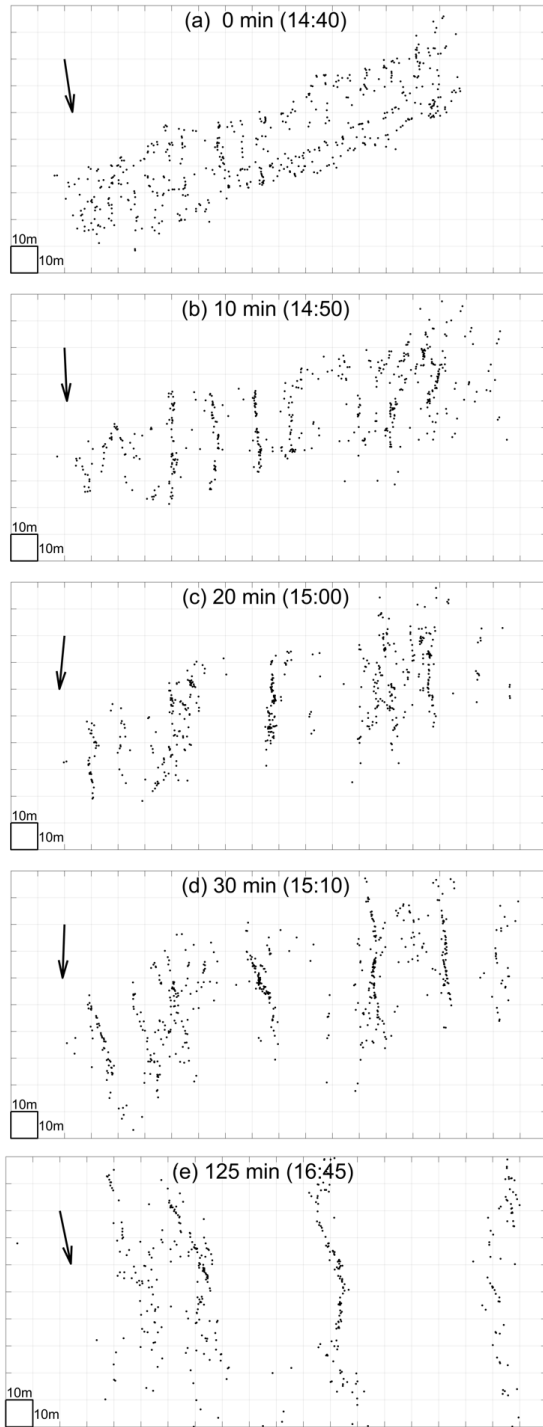
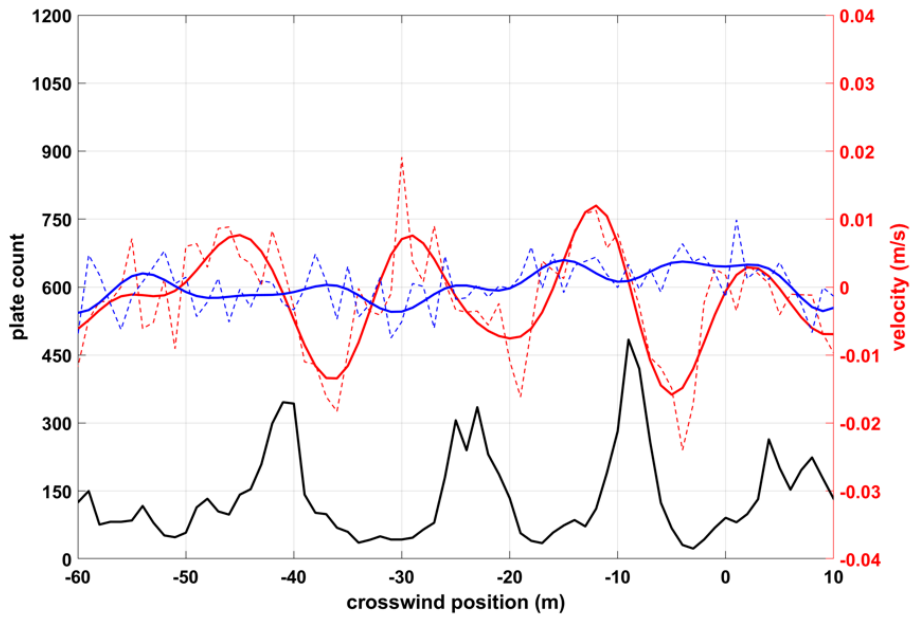
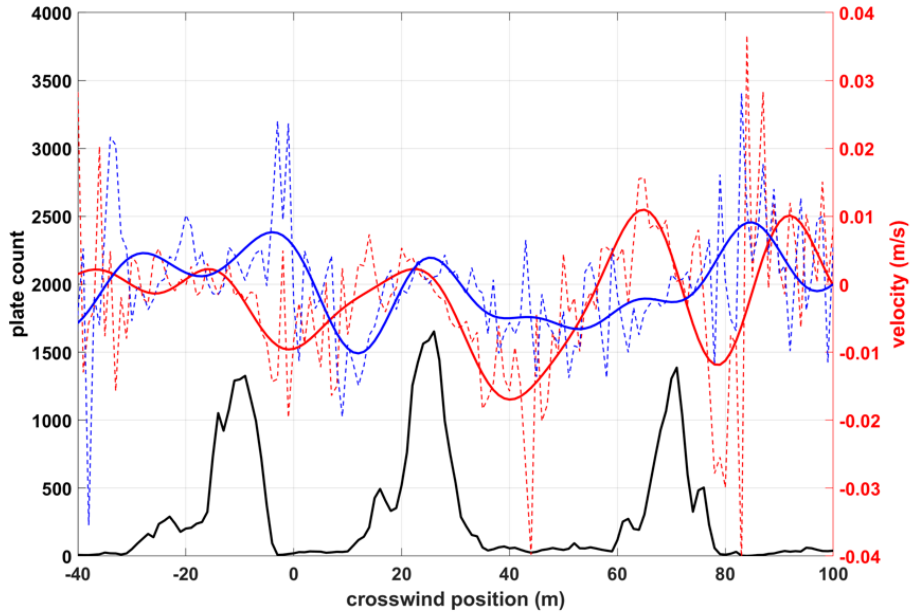


FIG. 5. Relatively rectified plate positions after 0, 10, 20, 30, and 125 minutes, respectively, (a) – (e). Black arrows show wind direction inferred from the heading of the aerostat, which was designed to point into the wind. Grid spacing is 10 m in both directions. An animated version of this figure is included as supplemental material in the online version of this paper.

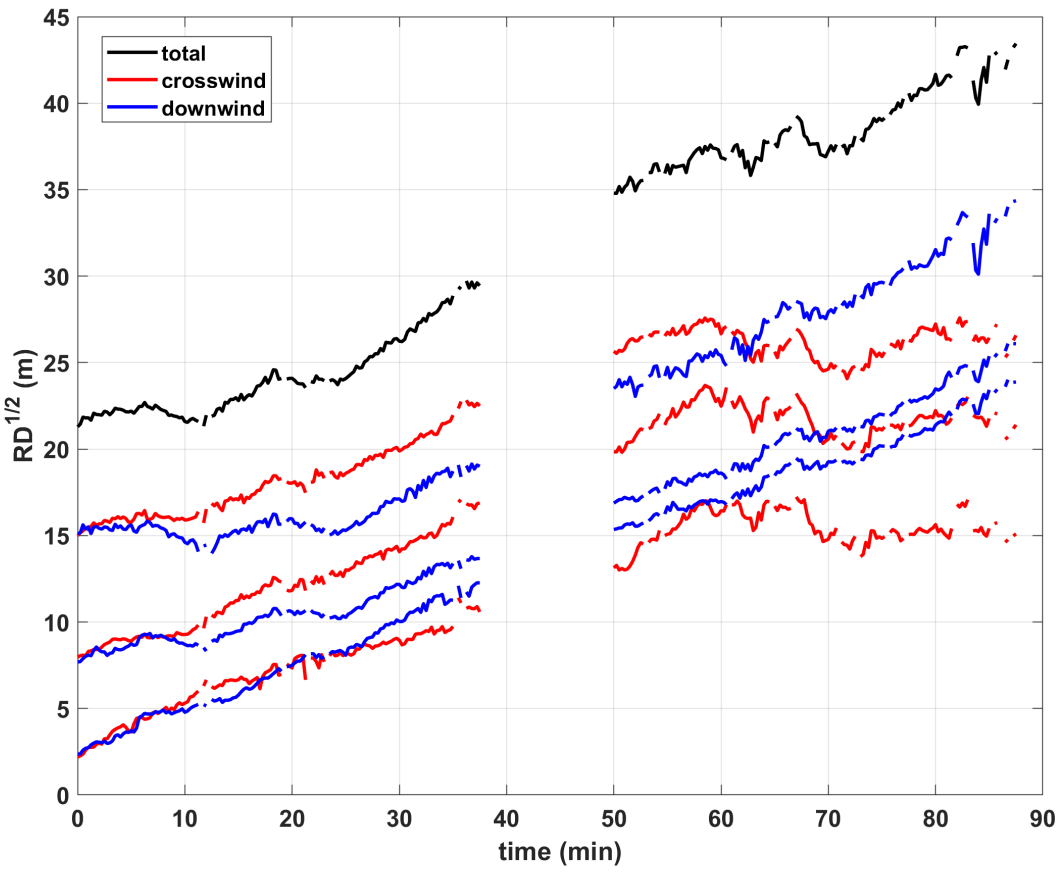


(a)

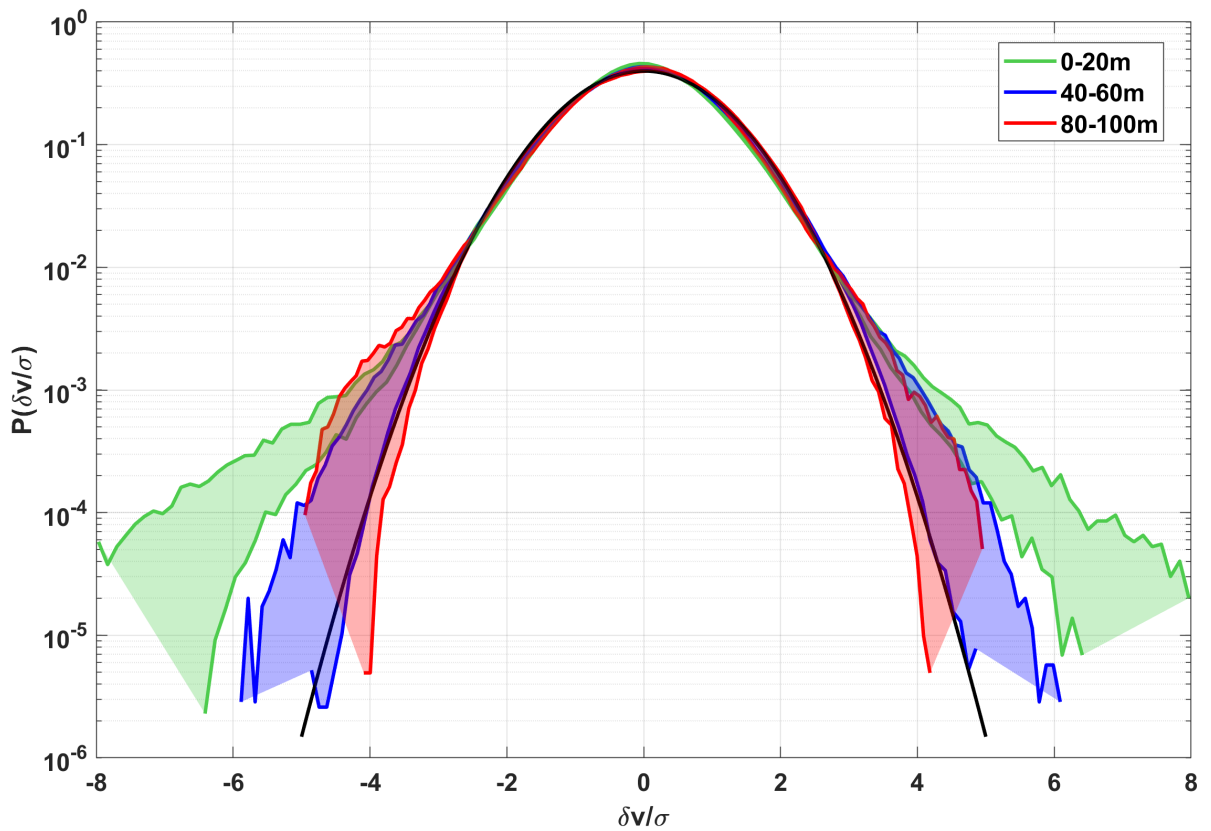


(b)

FIG. 6. Binned cumulative plate count (black), average crosswind velocity (red-dashed), and average downwind velocity (blue-dashed) as functions of crosswind position, for the first 10 min in (a), and for 50-90 min in (b). The corresponding solid curves are low-pass filtered velocities, with cut-off at 10 m for (a) and cut-off at 20 m for (b).



819 FIG. 7. Relative dispersion as a function of time for initially isotropic pair distributions. Average over all
 820 directions and scales (black), in the crosswind direction (red), and in the downwind direction (blue). Gaps
 821 reflect frames that could not be successfully processed.



822 FIG. 8. Normalized PDFs of longitudinal velocity increments for 3 separation distance bins. Uncertainty is
 823 shown (shading) for maximum linking distances of 1.7 – 3.4 m, which correspond to maximum velocities of 11
 824 – 22 cm/sec relative to the mean. A normalized Gaussian is indicated by the black curve.

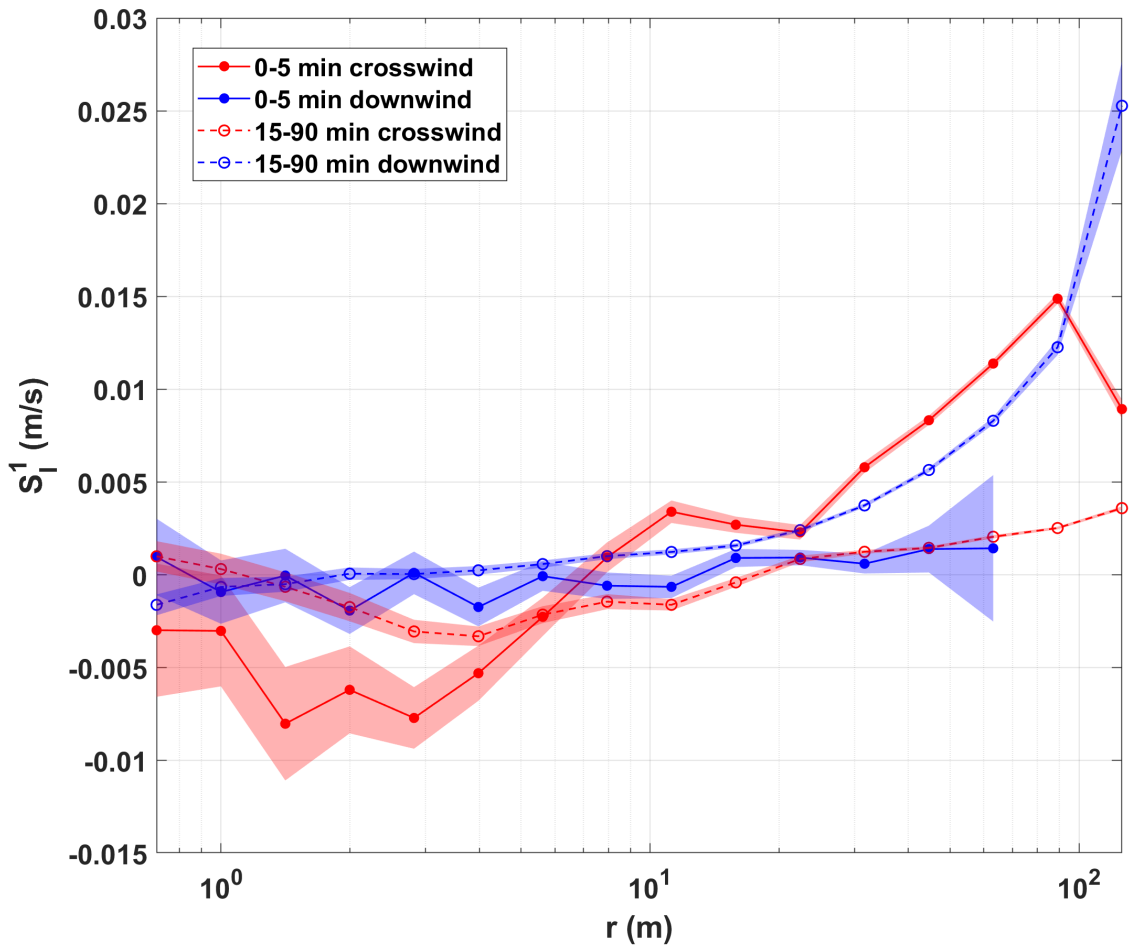


FIG. 9. Longitudinal first-order structure function for crosswind (red) and downwind (blue) components, subsampled at early (solid) and late (dashed) times. Shaded regions are 95% confidence intervals determined from standard error calculations.

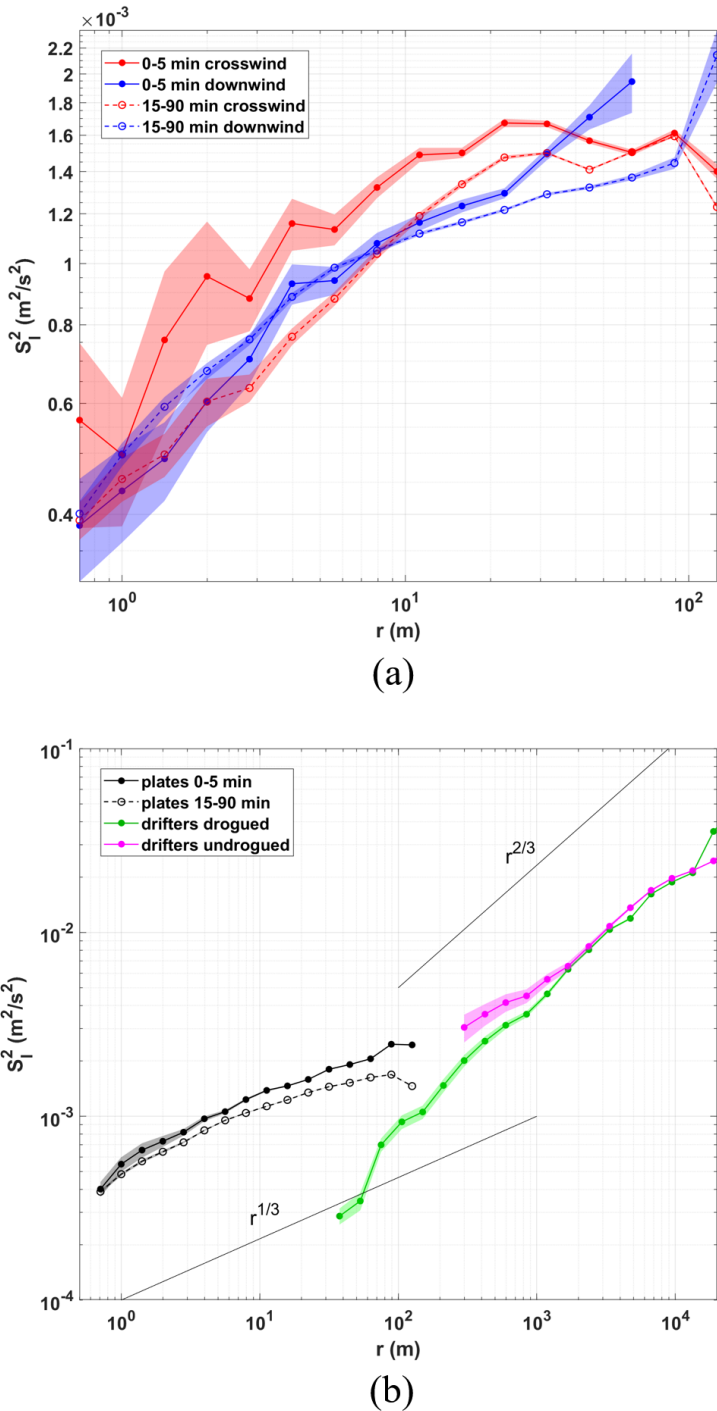
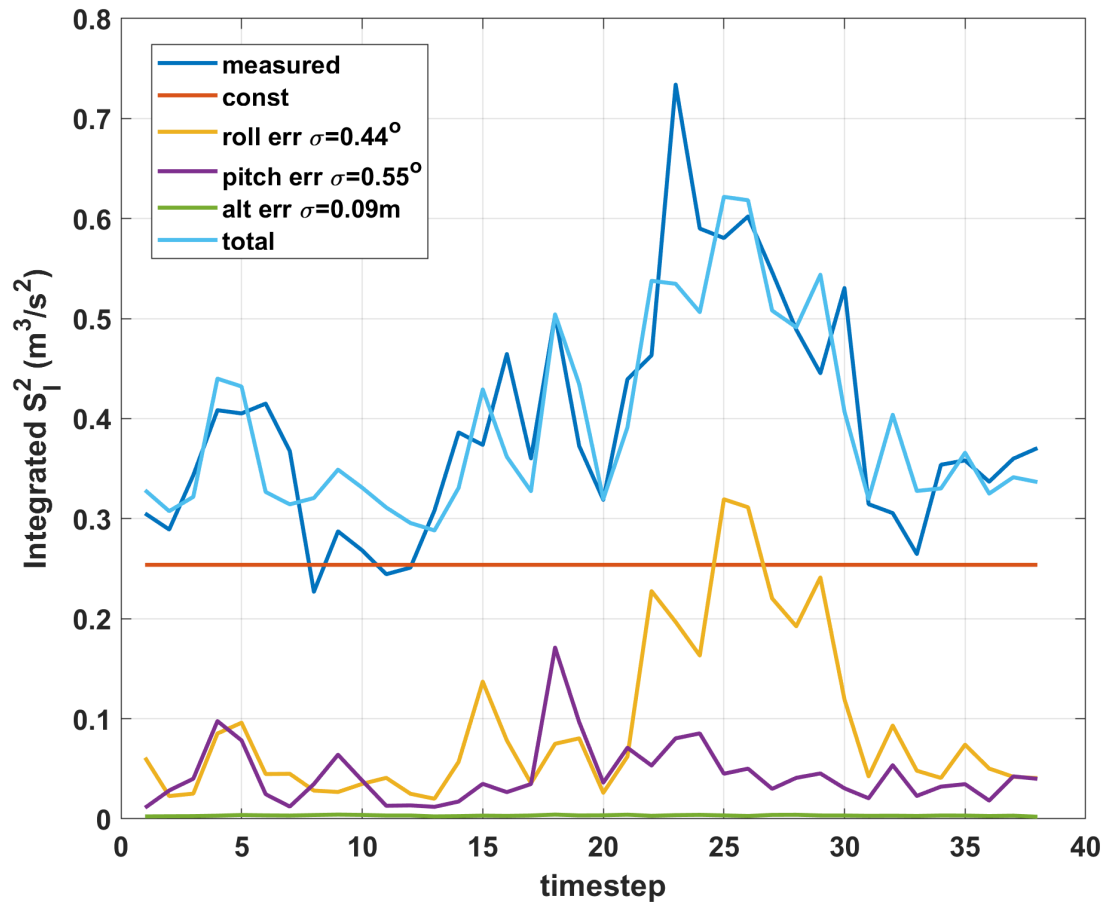


FIG. 10. Longitudinal second-order structure function. (a) Crosswind (red) and downwind (blue) components, subsampled at early (solid) and late (dashed) times. (b) For early-time (solid black) and late-time (dashed black) plates, plus drogued (green) and undrogued (magenta) drifters. Shaded regions are 95% confidence intervals determined from standard error calculations.



832 FIG. 11. Integrated second-order structure function with error (dark blue) as a function of sampling window
 833 τ (5-frame average) and the best fit for the individual components and their sum of the right-hand side of (A17),
 834 as computed over 38 sampling windows.

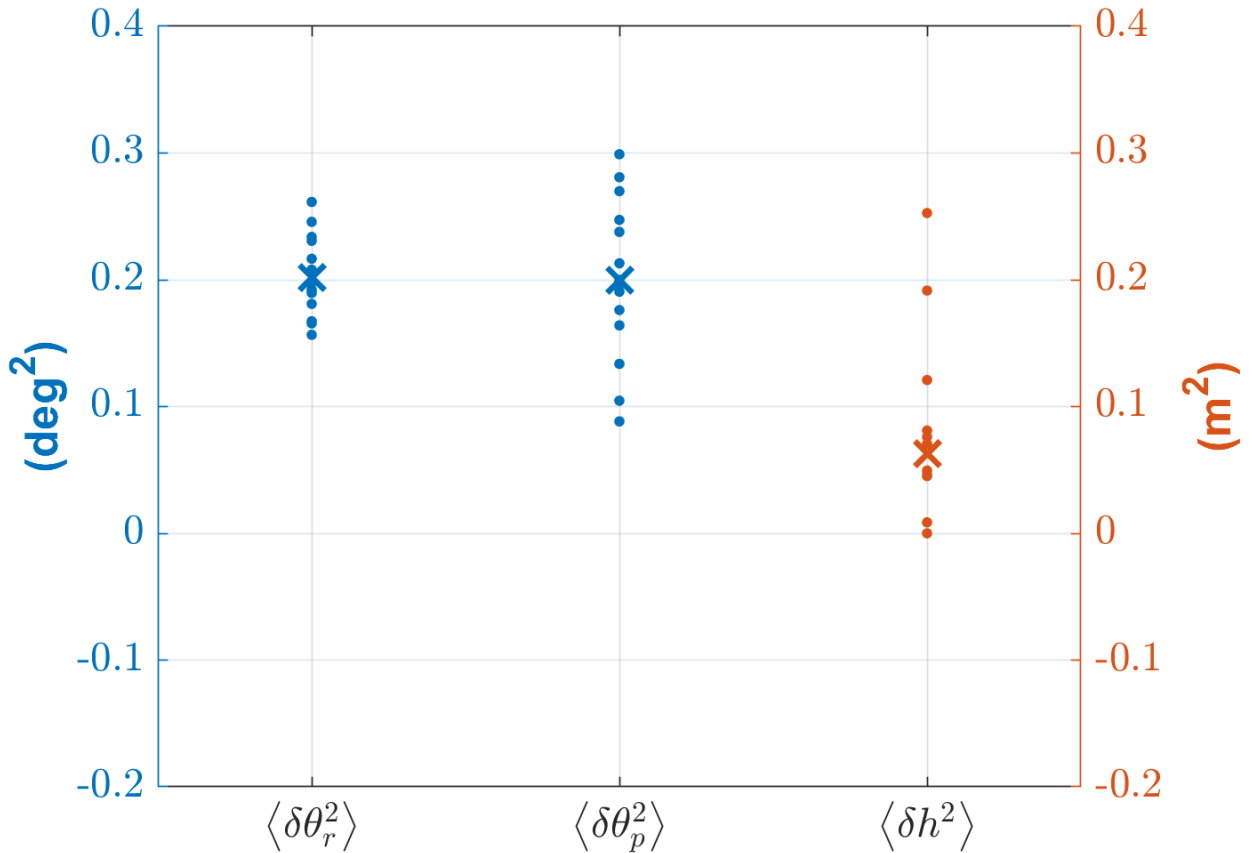


FIG. 12. Different estimates of the error statistics $\langle \delta h^2 \rangle$, $\langle \delta\theta_r^2 \rangle$, and $\langle \delta\theta_p^2 \rangle$ of altitude, roll, and pitch, respectively, from 15 fittings. Mean values are indicated by 'x's.